

Article

Use of Logistic Regression for Forecasting Short-Term Volcanic Activity

William N. Junek ^{1,*}, W. Linwood Jones ¹ and Mark T. Woods ²

¹ Central Florida Remote Sensing Laboratory, School of Electrical Engineering and Computer Science, University of Central Florida, Box-162450, Orlando, FL 32816-2450, USA; E-Mail: ljones@ucf.edu

² Graduate Faculty Scholar, School of Electrical Engineering and Computer Science, University of Central Florida, Box-162450, Orlando, FL 32816-2450, USA; E-Mail: mtewoods@earthlink.net

* Author to whom correspondence should be addressed; E-Mail: wjunek@knights.ucf.edu; Tel.: +1-407-823-6603; Fax: +1-407-868-1035.

Received: 15 May 2012; in revised form: 28 July 2012 / Accepted: 7 August 2012 /

Published: 22 August 2012

Abstract: An algorithm that forecasts volcanic activity using an event tree decision making framework and logistic regression has been developed, characterized, and validated. The suite of empirical models that drive the system were derived from a sparse and geographically diverse dataset comprised of source modeling results, volcano monitoring data, and historic information from analog volcanoes. Bootstrapping techniques were applied to the training dataset to allow for the estimation of robust logistic model coefficients. Probabilities generated from the logistic models increase with positive modeling results, escalating seismicity, and rising eruption frequency. Cross validation yielded a series of receiver operating characteristic curves with areas ranging between 0.78 and 0.81, indicating that the algorithm has good forecasting capabilities. Our results suggest that the logistic models are highly transportable and can compete with, and in some cases outperform, non-transportable empirical models trained with site specific information.

Keywords: logistic regression; eruption forecasting; event tree

1. Introduction

Volcanism combines complex geophysical and geochemical processes that vary in composition, duration, and intensity from location to location and episode to episode. Therefore, successful eruption

forecasting will only be achieved through the use of methods that simultaneously weigh empirical experience and real time interpretation of processes [1]. Event trees have proven to be useful tools for forecasting volcanic activity [2–4]. In 2002, Newhall and Hoblitt outlined a generic event tree structure for forecasting various types of volcanic activity and associated hazards. This process has since been adopted and improved upon by a variety of researchers to forecast volcanic activity at various locations throughout the world [5–12]. These event tree implementations require probability density functions to be manually derived on a volcano-by-volcano basis. This means every volcano being monitored will have a unique and unvalidated set of statistical functions driving its prediction process. As a result, each instance of the algorithm will use subjectively selected detection thresholds that possess a unique and unquantified false alarm rate.

This research initiative aims to improve and standardize the event tree forecasting process. The method employed here also uses Newhall and Hoblitt's generic event tree infrastructure. However, we have augmented its decision making process with a suite of empirical statistical models that are derived through logistic regression. Each model is constructed from a geographically diverse dataset that was assembled from a collection of historic volcanic unrest episodes. The dataset consists of monitoring measurements (e.g., seismic), source modeling results, and historic eruption activity information. The regression uses a generalized linear model routine (GLMR) that assumes a binominal response variable and employs a logit linking function. This process allows for trends in the relationship between modeling results, monitoring data, historic information, and the known outcome of the events to drive the formulation of the statistical models. It yields a static set of logistic models that weight the contributions of empirical experience and monitoring data relative to one another. They estimate the probability of a particular event occurring based on the current values of a set of predefined explanatory variables, are highly transportable, and do not need to be redefined for each volcano being monitored. This provides a simple mechanism for simultaneously accounting for the geophysical changes occurring within the volcano and the historic behavior of analog volcanoes in short-term forecasts. In addition, a rigorous cross validation process is used to document the algorithm's performance, identify optimum detection thresholds, and quantify false alarm rates. The methodology is easily extensible, where recalibration can be performed or new branches added to the decision making process with relative ease. Such a system could aid federal, state, and local emergency management officials in determining the proper response to an impending eruption and can be easily deployed by a National Volcano Early Warning System (NVEWS).

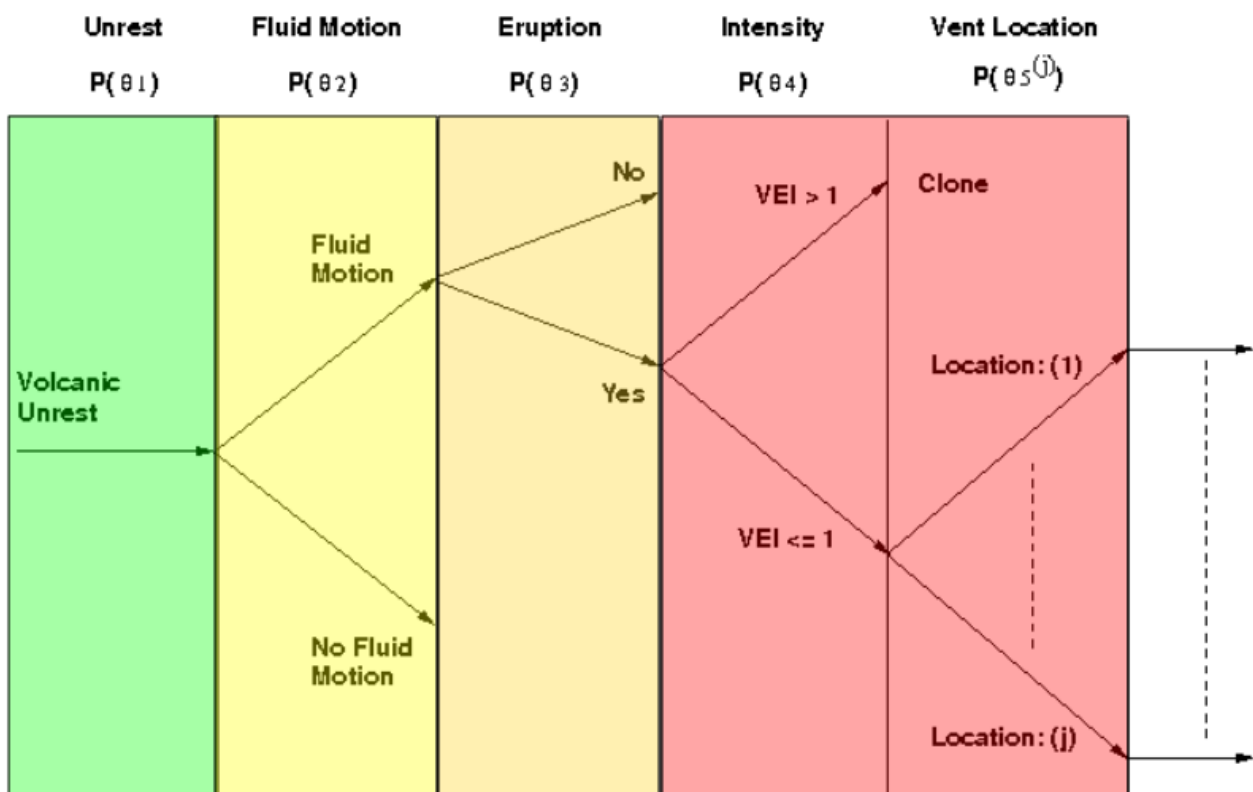
This paper is organized into several sections. It begins with an overview of the volcanic eruption forecasting algorithm, logistic models, and cross validation analysis. The next section provides a detailed discussion of forecasts generated by the algorithm. The final section discusses the conclusions that can be drawn from this work and provides an overview of future research initiatives that may improve the algorithm's performance.

2. Eruption Forecasting Algorithm

An event tree is a decision making framework that estimates the probability of a set of pre-defined events using a tree like decision making process. Each branch or node of the tree represents a set of

possible outcomes for a particular event, which increase in specificity with each step. Progression to the next branch is accomplished when the probability estimate for the preceding node exceeds a pre-defined threshold. Our algorithm is rooted in a general state of unrest and grows to forecast volcanic activity in increasing detail, such as the probability of eruption, intensity, and location.

Figure 1. Schematic representation of the event tree, where the clone label indicates the tree structure at that point is identical to that below. The color code represents the USGS ground-based hazard declarations and are superimposed over their respective event tree branch.



The event tree utilized in this research is shown in Figure 1. Each node estimates the conditional probability for a specific event via Bayes theorem, which is defined as

$$P(n|n - 1) = \frac{P(n, n - 1)}{P(n - 1)} = \frac{P(n - 1|n)P(n)}{P(n - 1|n)P(n) + P(n - 1|n')P(n')} \tag{1}$$

where $P(n - 1|n)$ is the likelihood, $P(n)$ is the prior probability, $P(n - 1)$ is the marginal probability, $P(n|n - 1)$ is the posterior probability, the prime symbol represents the complement, and n is the event tree node. Our event tree implementation is comprised of the following nodes:

- Node 1. *Unrest: Does the geophysical activity at the selected volcano exceed a predetermined threshold?* Geophysical activity includes heightened seismicity or surface deformation. If the amount of unrest exceeds a predefined threshold, the decision making process progresses to the

next branch, otherwise it terminates and restarts when new data are available. If the predefined threshold is exceeded, the probability that unrest is occurring equals one, which is given by

$$P(\Theta_1) = P(1) = \begin{cases} 0 & \text{if } \nu_1 = 0 \\ 1 & \text{if } \nu_1 > 0 \end{cases} \quad (2)$$

where ν_1 is the summation of several explanatory variables that are defined in Section 2.3.

- Node 2. *Magmatic Intrusion: Is the observed unrest the result of a magmatic intrusion?* Fluid motion can be detected from the presence of heightened levels of seismicity having specific spectral characteristics or continuous or rapidly varying surface deformation. Possible causes of unrest that are not related to fluid motion or not indicative of an impending eruption include tectonic and geothermal activity. If the unrest is related to fluid motion, the process progresses to the next branch, otherwise it terminates and restarts when new data are available. The probability that an intrusive event is occurring is given by

$$P(\Theta_2) = P(2|1) = \frac{P(1|2)P(2)}{P(1|2)P(2) + P(1|2')P(2')} \quad (3)$$

where $P(2)$ is defined as

$$P(2) = P(\text{Intrusion}|X_{2,N}) \quad (4)$$

and $X_{2,N}$ is a node specific set of N independent explanatory variables described in Section 2.4.

- Node 3. *Eruption: Does the detected fluid motion have the potential to reach the surface and cause an eruption?* If the source of the unrest is a magmatic intrusion with associated seismicity, the probability that the fluid will reach the surface may be high if that particular volcano has a historically high eruption frequency. If the observed, modeled, and historic information support this hypothesis, the algorithm moves to the next branch, otherwise it terminates and restarts when new data are available. The probability that an eruption will occur is given by

$$P(\Theta_3) = P(3|2) = \frac{P(2|3)P(3)}{P(2|3)P(3) + P(2|3')P(3')} \quad (5)$$

where $P(3)$ is defined as

$$P(3) = P(\text{Eruption}|X_{3,N}) \quad (6)$$

and $X_{3,N}$ is a node specific set of N independent explanatory variables described in Section 2.4.

- Node 4. *Intensity: Will the eruption intensity exceed a VEI of 1?* The determination of the intensity will be driven by the training dataset defined in Table 1. The probability of the eruption's intensity exceeding a Volcanic Explosivity Index, (VEI), of 1 is given by

$$P(\Theta_4) = P(4|3) = \frac{P(3|4)P(4)}{P(3|4)P(4) + P(3|4')P(4')} \quad (7)$$

where $P(4)$ is defined as

$$P(4) = P(\text{VEI} > 1|X_{4,N}) \quad (8)$$

and $X_{4,N}$ is a node specific set of N independent explanatory variables described in Section 2.4.

- Node 5. *Vent Location: Where is the eruption likely to occur?* A vent location probability map is generated and the area with the highest probability of occurrence is identified as the likely eruption location. Given that the previous conditions are satisfied, the most probable vent location may be those with collocated surface deformation and seismicity. The probability of an eruption occurring at any location in a specified area is given by

$$P(\Theta_5^{(j)}) = P(5^{(j)}|4) = \sum_{j=1}^J \frac{P(4|5^{(j)})P(5^{(j)})}{P(4|5^{(j)})P(5^{(j)}) + P(4|5'^{(j)})P(5'^{(j)})} \tag{9}$$

where J is the total number of probable vent locations, j is the location under consideration, and $P(5)$ is defined in Section 2.5.

The probability of an event occurring at a particular event tree node is defined as

$$P(\Theta) = \prod_1^l P(\Theta_l) \tag{10}$$

where l is the event tree node for which the probability is being calculated. For example, the probability of an eruption occurring at the j^{th} location is calculated from the product, $P(\Theta_1) P(\Theta_2) P(\Theta_3) P(\Theta_4) P(\Theta_5^{(j)})$, whereas the probability of an eruption occurring at a given volcano is estimated by $P(\Theta_1) P(\Theta_2) P(\Theta_3)$.

Table 1. Raw logistic regression training data.

| Episode | | Response Variable | | | | Independent Variable | | | | |
|---------|-------------------------------------|-------------------|----|----|----|----------------------|-----------|------|-----|---------|
| Year | Volcano | VEI | Er | In | MM | TNE | TCSM | Days | TEH | Ref. |
| 1993 | Medicine Lake ^(2,3,4) | 0 | 0 | 0 | 0 | 115 | 6.0e + 21 | 2492 | 1 | [13] |
| 1993 | Makushin ^(3,4) | 0 | 0 | 1 | 1 | 0 | 0 | 365 | 12 | [14] |
| 1994 | Hengill ^(2,3,4) | 0 | 0 | 1 | 1 | 63450 | 7.7e + 23 | 1607 | 0 | [15] |
| 1995 | Trident ^(2,3,4) | 0 | 0 | 1 | 1 | 69 | 3.2e + 19 | 137 | 13 | [16] |
| 1996 | Lassen Peak ^(2,3,4) | 0 | 0 | 0 | 0 | 110 | 3.4e + 21 | 1460 | 1 | [17] |
| 1996 | Eyjafjallajökull ^(2,3,4) | 0 | 0 | 1 | 1 | 144 | 5.2e + 19 | 114 | 2 | [18] |
| 1996 | Akutan ⁽²⁾ | 0 | 0 | 1 | 1 | 1194 | 7.6e + 22 | 32 | 34 | [19] |
| 1996 | Iliamna ^(2,3,4) | 0 | 0 | 1 | 1 | 1477 | 2.1e + 21 | 382 | 2 | [20] |
| 1996 | Peulik ^(2,3,4) | 0 | 0 | 1 | 1 | 0 | 0 | 365 | 2 | [21,22] |
| 1997 | Kilauea ^(2,3) | 1 | 1 | 1 | 0 | 1869 | 1.9e + 22 | 20 | 63 | [23] |
| 1998 | Kiska ^(2,3,4) | 0 | 0 | 0 | 0 | 0 | 0 | 365 | 3 | [24] |
| 1998 | Grimsvötn ^(2,3,4) | 3 | 1 | 1 | 1 | 31 | 9.4e + 20 | 10 | 29 | [25] |
| 1999 | Shishaldin ^(2,3,4) | 3 | 1 | 1 | 0 | 688 | 9.0e + 22 | 42 | 34 | [26] |
| 1999 | Fisher ^(2,3,4) | 0 | 0 | 0 | 1 | 0 | 0 | 365 | 1 | [27] |
| 2000 | Katla ^(2,3,4) | 0 | 0 | 1 | 1 | 12460 | 1.2e + 23 | 2190 | 4 | [28] |
| 2000 | Kilauea ^(2,3,4) | 0 | 0 | 0 | 0 | 48 | 5.8e + 20 | 13 | 63 | [29] |
| 2000 | Three Sisters ^(2,3,4) | 0 | 0 | 1 | 1 | 0 | 0 | 1460 | 1 | [22] |

Table 1. Cont.

| Episode | | Response Variable | | | | Independent Variable | | | | |
|---------|-------------------------------------|-------------------|---|---|---|----------------------|-------------|-------|-----|---------|
| 2000 | Hekla ^(2,3,4) | 3 | 1 | 1 | 1 | 196 | 3.4e + 20 | 15 | 9 | [30,31] |
| 2000 | Eyjafjallajökull ^(2,3,4) | 0 | 0 | 1 | 1 | 170 | 4.1e + 20 | 365 | 2 | [32] |
| 2001 | Etna ^(2,3,4) | 2 | 1 | 1 | 1 | 414 | 1.0e + 23 | 28 | 115 | [33] |
| 2001 | Okmok ⁽⁴⁾ | 0 | 0 | 0 | 1 | 19 | 8.1e + 21 | 2 | 16 | [34] |
| 2001 | Aniakchak ^(2,3,4) | 0 | 0 | 0 | 1 | 13 | 5.8e + 20 | 64 | 1 | [35] |
| 2002 | Hood ^(2,3,4) | 0 | 0 | 0 | 0 | 86 | 7.8e + 22 | 60 | 2 | [36] |
| 2002 | Etna ^(2,3,4) | 3 | 1 | 1 | 1 | 353 | 2.1e + 23 | 94 | 115 | [37] |
| 2003 | Veniaminof ⁽²⁾ | 2 | 1 | 1 | 1 | 103 | 6.2e + 20 | 1050 | 22 | [38] |
| 2004 | Grimsvötn ^(2,3,4) | 3 | 1 | 0 | 0 | 920 | 6.3e + 21.9 | 490 | 29 | [39] |
| 2004 | Spurr ^(3,4) | 0 | 0 | 0 | 0 | 2743 | 5.1e + 20 | 239 | 2 | [40,41] |
| 2004 | Etna ^(2,3,4) | 1 | 1 | 1 | 1 | 156 | 4.8e + 21 | 186 | 115 | [42] |
| 2004 | Saint Helens ^(2,3,4) | 2 | 1 | 1 | 1 | 1094 | 1.5e + 23 | 21 | 14 | [43] |
| 2005 | Augustine ^(2,3,4) | 3 | 1 | 1 | 1 | 2007 | 3.1e + 20 | 80 | 9 | [44] |
| 2006 | Korovin ^(2,3,4) | 1 | 1 | 0 | 1 | 377 | 1.4e + 21 | 329 | 7 | [45,46] |
| 2007 | Pavlof ⁽²⁾ | 2 | 1 | 1 | 0 | 2 | 8.8e + 18 | 30 | 39 | [47] |
| 2007 | Upptyppingar ^(2,3,4) | 0 | 0 | 1 | 0 | 3124 | 6.5e + 20 | 133 | 0 | [48] |
| 2008 | Yellowstone ^(2,3) | 0 | 0 | 1 | 1 | 2594 | 6.9e + 22 | 49 | 0 | [49] |
| 2008 | Paricutin ^(2,3,4) | 0 | 0 | 0 | 0 | 0 | 0 | 21900 | 1 | [50] |
| 2008 | Hengill | 0 | 0 | 0 | 0 | 3309 | 1.1e + 24 | 10 | 0 | [51] |
| 2008 | Okmok ^(2,3,4) | 4 | 1 | 1 | 1 | 464 | 4.9e + 21 | 100 | 16 | [34,52] |
| 2008 | Kasatochi ^(2,3,4) | 4 | 1 | 1 | 0 | 1489 | 7.4e + 24 | 22 | 1 | [53] |
| 2009 | Redoubt ^(2,3,4) | 3 | 1 | 1 | 1 | 4219 | 3.9e + 21 | 365 | 6 | [31] |
| 2010 | Eyjafjallajökull ^(2,3,4) | 4 | 1 | 1 | 1 | 4019 | 1.1e + 22 | 100 | 2 | [54] |

The event tree was adapted to issue warnings according to the United States Geological Survey (USGS) ground-based volcanic hazard system. Our system assigns colors ranging from green to red to a particular volcano according to its current eruption hazard condition, where green = normal, yellow = advisory, orange = watch, and red = warning. Figure 1 shows the color code assignments relative to each stage of the event tree. The final color designation is set according to the point in the algorithm where processing is terminated. For example, if the algorithm is activated by a new unrest episode and is not allowed to progress past the eruption node, because the probability of occurrence does not exceed a predefined decision threshold, then the final hazard level is set to orange. However, if the algorithm were to progress to the intensity node the hazard level is set to red.

2.1. Logistic Regression

Logistic regression is a statistical modeling method used to analyze multivariate problems [55–57]. It attempts to describe the complex relationship between a set of independent explanatory variables and a response variable. This popular modeling approach is used extensively in medical research, bioinformatics, and marketing analysis [58]. It has also found use in geophysical applications, such as the prediction of landslides and rain rate [59,60].

The logistic function, $f(z)$, is given by

$$f(z) = \frac{1}{1 + e^{-z}} \quad (11)$$

where z is a value computed from a logistic model. The range of $f(z)$ is bound between 0 and 1 over $\pm\infty$. Unlike other modeling techniques, a probability between 0 and 1 is guaranteed with logistic regression regardless of the value of z . The logistic model is the weighted summation of a set of explanatory variables, which is defined as

$$z = \beta_0 + \sum_{m=1}^N \beta_m X_m \quad (12)$$

where β_0 is a constant (intercept), β_m are the weighting (regression) coefficients, and X_m are the explanatory variables. Values of β_0 and β_m are determined through maximum likelihood estimation via a GLMR. This requires a training dataset consisting of a collection of observations that relate the outcome of a particular event to the explanatory variables.

Using this technique, we derived a suite of logistic models to compute the prior probability for the n^{th} event tree node. These models are defined as the conditional probability

$$P(n) = P(\theta_n = 1 | X_{n,1} \dots X_{n,N}) = \frac{1}{1 + e^{-z_n}} \quad (13)$$

where θ_n is the outcome (*i.e.*, 1 or 0) of the event represented by the n^{th} node and z_n is its respective logistic model. Weighting coefficients for each logistic model are described in Section 2.4.

The goodness-of-fit (G) of a logistic model is often assessed using a likelihood ratio test [56]. The test statistic is derived from the difference between the deviance, $-2\ln(L_n)$, of the null and full models, where the null model is simply a constant with no associated explanatory variables. The deviance is similar to the residual sums of squares metric from ordinary least squares regression in the sense that it attempts to estimate the discrepancy between the modeled and observed data. Thus, the quality of the regression model decreases with increasing deviance. Here G is estimated via the ratio

$$G = \chi^2 = -2\ln\left(\frac{L_{null}}{L_{full}}\right) \quad (14)$$

where L_{null} and L_{full} are the likelihoods of the null and full models. The test statistic is χ^2 distributed, where its degrees of freedom, df , are equivalent to the number of constrained predictors (explanatory variables) in the logistic model. Statistical significance of the difference is estimated using a hypothesis test which compares the p-value of the test statistic to a predefined significance level (0.05), where the null hypothesis states the null model fits the data better than the full model. If there is strong evidence against the null hypothesis (*e.g.*, $p < 0.05$), then it can be rejected in favor of the full model.

2.2. Training Data

A database comprised of monitoring data, source modeling results, and historic eruption information from a series of volcanic unrest episodes is required for deriving the logistic model coefficients. Unfortunately, no such database existed in the public domain at the time of this study. Therefore, one had to be constructed for this research. Ideally, a large and diversified set of data is desired for identifying the set of explanatory variables that will produce the most robust logistic model. Moreover, it is also desirable to identify a large number of events that either culminate or fail to culminate into an eruption. However, published accounts of volcanic unrest events vary greatly in detail and do not contain a consistent set of observations. This problem is exasperated by the fact that events which eventually result in an eruption tend to be published, while those that fail are not. This has artificially biased the open literature toward eruptive events as opposed to those that eventually fail [61]. As a result, only a small set of unrest events with known sources and a consistent set of explanatory variables could be identified for this research.

The database constructed for this work is listed in Table 1. It is a collection of unrest events with a consistent set of observations whose causes were identified through source modeling. The 40 events in the database were gathered from various volcanoes in Northern America, Iceland, and Italy. For an event to be included in the database, a seismic catalog and modeling results that identify the source of the unrest must be available. These data were acquired from a combination of journal articles, technical reports, conference papers, and open seismic catalogs that are made freely available to the public by a number of organizations (e.g., USGS, ANSS, Icelandic Meteorological Institute) via the internet. It is assumed that this collection of events represent a random sample of volcanic activity in the northern hemisphere and is representative of this population.

Table 1 consists of eleven columns. The first two columns list the episode year and volcano of origin. Column three is the event's (*VEI*). The fourth column, (*Er*), specifies whether the event culminated in an eruption, where true (eruption) and false (no eruption) outcomes are represented by a 1 or 0. The cause of the unrest is listed in column five, (*In*), where a value of 1 or 0 states whether the source is a magmatic intrusion or not. Source modeling results are listed in column six, (*MM*), where a value of 1 or 0 states if the source of the unrest can be modeled as a magmatic intrusion or not. The total number of earthquakes occurring over the course of the episode is listed in column seven, (*TNE*). An estimate of the total cumulative seismic moment generated throughout the episode, (*TCSM*), is listed in column eight. The duration of each episode in terms of days is listed in column nine, (*Days*). The total number of eruptions at a particular site over the last 211 years is listed in column ten, (*TEH*). This time span represents the extent of the Smithsonian Institute (SI) global volcanism database of eruptions that are known to have occurred in modern history (post 1800) [62]. It is meant to prevent overestimation of the probability of eruption at sites that typically display high levels of geologic activity but rarely erupt. The Yellowstone caldera is a prime example of where such a term is necessary. If historic eruption activity is not accounted for at Yellowstone, forecasts would show that an eruption is imminent (probability of eruption = 1.0) inside the caldera on an almost continuous basis. When historic eruptive activity is taken into consideration, the probability of eruption is adjusted to account for long periods of non-eruptive behavior. Finally the source of the information listed in each row is referenced in column eleven.

Superscripts above the volcano name represent that sample’s participation in the derivation of logistic coefficients for each node. Note that the logistic regression is performed after the *TNE* and *TCSM* columns are transformed to average values per day and the normalization factor $(1e20dyn - cm)$ is applied to the cumulative seismic moment estimates.

2.3. Node 1: Detection of Volcanic Unrest

Anomalous geologic activity (e.g., volcanic unrest) is detected using the method described in [63]. Historic information collected by a variety of multidisciplinary remote and in-situ sensing techniques is used to identify activity that is markedly different (i.e., outliers) from past behavior. Discipline specific outlier thresholds are derived from

$$Outlier\ Threshold = Q_3 + c(Q_3 - Q_1) \tag{15}$$

where c is a constant, Q_1 and Q_3 are the first and third quartiles of the sample distribution, and $(Q_3 - Q_1)$ is the interquartile range [64]. Unique thresholds are derived empirically on a volcano-by-volcano and monitoring discipline basis using Equation 15, where c is set empirically for each monitoring discipline.

The severity of the anomaly is estimated from the weighted summation of a collection of binary variables. The general form of the severity estimate is defined as

$$\nu_1 = \sum_{m=1}^N \beta_m X_m \tag{16}$$

where β_m are weighting coefficients and X_m are binary variables that are toggled from 0 to 1 when measurements from their respective monitoring discipline exceeds its outlier detection threshold. Here the functional form of Equation 16 is expressed as

$$\nu_1 = 0.25(X_{sr} + X_{df} + X_{lm} + X_{md}) \tag{17}$$

where each binary variable is defined in Table 2. In this case, all variables are weighted equally ($\beta_m = 0.25$) to allow activation of the forecasting algorithm upon the detection of unrest by one or more monitoring techniques. Severity declarations are based on the number of simultaneous cross-disciplinary detections, where ν_1 values of 0.25, 0.50, 0.75, and 1.0 represent low, moderate, heightened, and extreme levels of unrest. This triggering mechanism differs from those described in previously published event tree implementations (e.g., [7]) through its use of outlier analysis for detection threshold estimation and the incorporation of source modeling information.

Table 2. Explanatory variable names, descriptions, and possible values for node 1.

| Explanatory Variable | Description | Value |
|----------------------|---------------------------|-------|
| X_{sr} | Seismicity Rate | 0/1 |
| X_{df} | Surface Deformation | 0/1 |
| X_{lm} | Large Magnitude | 0/1 |
| X_{md} | Model Indicates Intrusion | 0/1 |

2.4. Nodes 2–4: Intrusion, Eruption, and Intensity

Ideally, the regression uses many combinations of random samples from the population we are attempting to model. After many iterations, a distribution of parameter estimates, such as the sample mean or regression coefficients, can be produced and their true value estimated. In this case, however, there are no additional data available. Therefore, a bootstrapping approach is used to estimate the distribution of logistic model coefficients for nodes 2, 3, and 4 using selected subsets of data from Table 1.

Bootstrapping is a resampling technique that produces M datasets from a single set of random samples taken from a specific population. Each of the newly constructed datasets contains a random combination of samples that were drawn from the original dataset. Since a sample with replacement process is used, it is possible for each new dataset to contain multiple or no copies of any particular sample. Thus, the probability that a particular sample is selected for inclusion in a bootstrapped dataset each time a drawing is made is $1/N$, where N is the number of samples in the original dataset.

Model coefficients for each node were estimated from the distributions generated after 50,000 bootstrapped GLMR iterations. The distributions for each of the logistic model coefficient appears to be bimodal. The two distributions represent cases where the regression is either properly or ill constrained. Situations where the regression is ill constrained caused the GLMR to fail after reaching its maximum number of iterations, which results in a bogus set of model coefficients. Conversely, properly constrained cases represent runs where the GLMR converges to a solution within its maximum number of iterations. Therefore, the ill constrained results are rejected as outliers and the properly constrained distributions are retained and used to estimate logistic model information. In all cases, the median value of the truncated distributions are used to estimate the coefficients for each model.

The logistic models for nodes 2, 3, and 4 are shown in Equations 18–20 and a description of each explanatory variable is listed in Table 3. Node 3 (Equation 19) required an additional explanatory variable to account for the relationship between historic eruption activity and monitoring data. The likelihood ratio test for each model yielded p-values of 0.001, 0.014, and 0.007, which provides strong evidence against the null hypothesis for each node.

Table 3. Logistic model explanatory variable names, descriptions, and possible range of values.

| Explanatory Variable | Description | Value |
|----------------------|--|--------------|
| X_{MM} | Unrest consistent with intrusion model | 0 or 1 |
| X_{NE} | Average Number of Earthquakes Per Day | $0 - \infty$ |
| X_{CSM} | Average Normalized Cumulative Seismic Moment Per Day | $0 - \infty$ |
| X_{DAYS} | Episode Duration in Days | $0 - \infty$ |
| X_{ERH} | Average Eruption History | $0 - \infty$ |

The influence of the source modeling results (X_{MM}) on each logistic function is examined by setting all other explanatory variables equal to each other and plotting the model response for values ≥ 0 .

Figures 2–4 show that positive modeling results increase the probability of occurrence for each node. In addition, each plot shows that even in the absence of positive modeling results, episodes producing large numbers of earthquakes and/or releasing large amounts of seismic energy have a high probability of being generated by a magmatic intrusion. Moreover, they also show that the probability of an eruption is non-zero when all explanatory variables are equal to zero. This result is reassuring, since eruptions have been known to occur without any precursory activity or warning.

$$z_2 = -1.5618 + 2.6869(X_{MM}) + 0.3465(X_{NE}) - 0.0041(X_{CSM}) - 0.0001(X_{DAYS}) \quad (18)$$

$$z_3 = -3.4589 + 2.1401(X_{MM}) + 0.0056(X_{NE}) + 0.0023(X_{CSM}) - 0.0014(X_{DAYS}) + 12.8714(X_{ERH}) \quad (19)$$

$$z_4 = -1.7369 + 0.7924(X_{MM}) + 0.1293(X_{NE}) - 0.0006(X_{CSM}) - 0.0033(X_{DAYS}) \quad (20)$$

Figure 2. Logistic functions derived from bootstrapping process for the intrusion node, where the black and red curves represent $X_{MM} = 0$ and $X_{MM} = 1$. The transition of X_{MM} from 0 to 1 increases the probability of occurrence by 0.60, which is the difference between the black and red curves when all continuous input variables are equal to 0.

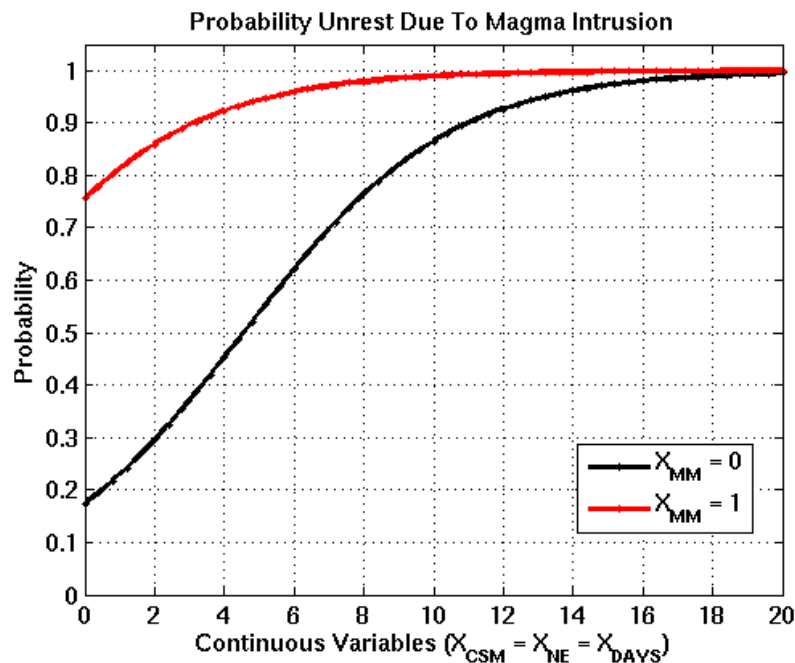


Figure 3. Logistic functions derived from bootstrapping process for the Eruption node, where the black and red curves represent $X_{MM} = 0$ and $X_{MM} = 1$. The transition of X_{MM} from 0 to 1 increases the probability of occurrence by 0.17, which is the difference between the black and red curves when all continuous input variables are equal to 0.

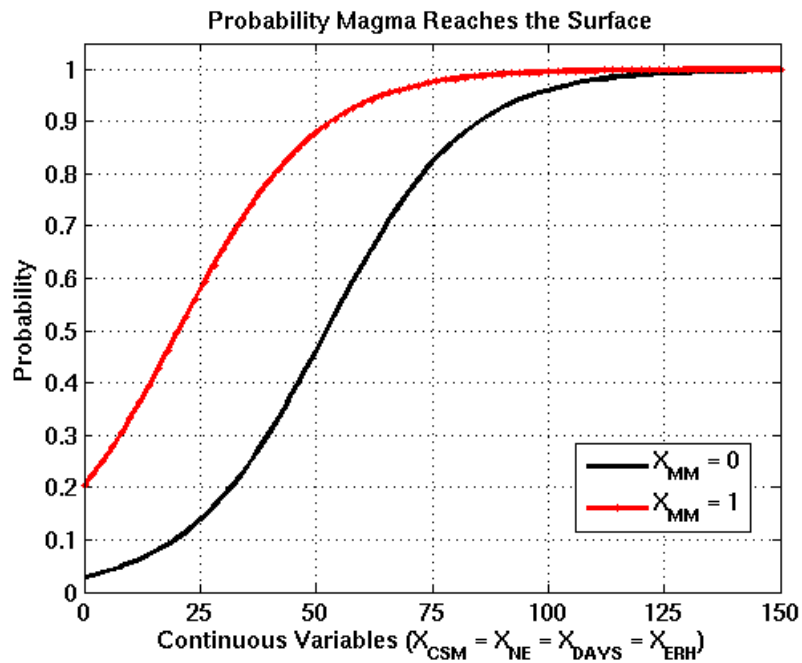
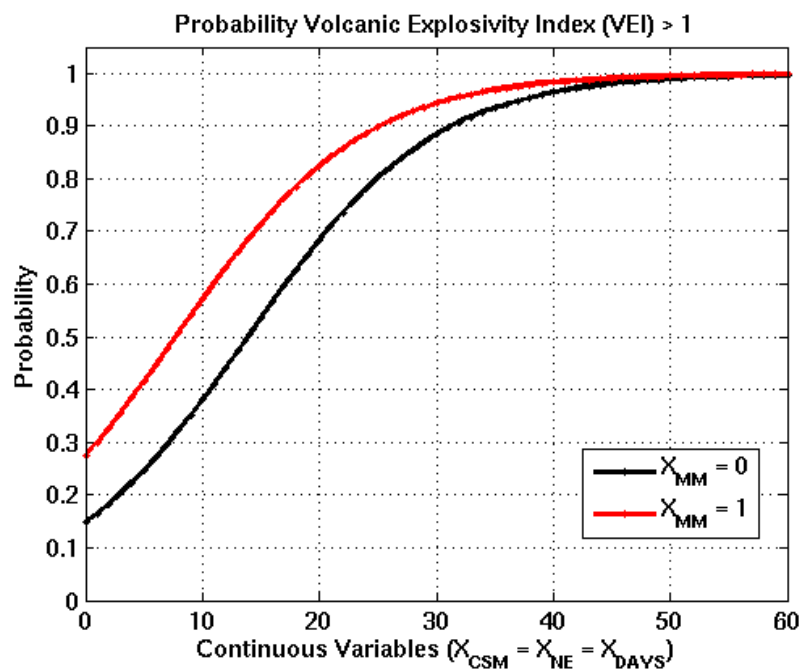


Figure 4. Logistic functions derived from bootstrapping process for the intensity node, where the black and red curves represent $X_{MM} = 0$ and $X_{MM} = 1$. The transition of X_{MM} from 0 to 1 increases the probability of occurrence by 0.13, which is the difference between the black and red curves when all continuous input variables are equal to 0.



2.5. Node 5: Vent Location

The spatial probability density function (PDF) for estimating the probability of vent formation (V) at the j^{th} location is derived from the data used for monitoring a particular volcanic center. Here the PDF is constructed from deformation data (X_{def}) and the spatiotemporal distribution of seismic epicenters (X_{seis}). Combining this information yields the expression

$$P(5^j) = P(V^j = 1 | X_{seis}^j, X_{def}^j) = \frac{X_{seis}^j + X_{def}^j}{\sum_{i=1}^J (X_{seis}^i + X_{def}^i)} \tag{21}$$

where J is the total number of probable vent locations under consideration. A detailed overview of the vent location algorithm employed in this paper is discussed in [65].

2.6. Cross Validation

Binary classification problems attempt to categorize the outcome of an event into one of two categories, either true (1) or false (0). This process can result in one of four possible outcomes that are defined as follows:

- *True Positive (TP)*: Predicted and actual results are 1 (Valid Detection)
- *False Positive (FP)*: Predicted result is 1, but actual result is 0 (False Alarm)
- *False Negative (FN)*: Predicted result is 0, but actual result is 1 (Missed Detection)
- *True Negative (TN)*: Predicted and actual results are 0 (Valid Non-detection)

The quality of a binary classifier is assessed through a receiver operating characteristic (ROC) analysis. A ROC curve is generated by plotting the prediction algorithm’s true positive rate (TPR or sensitivity) versus its false positive rate (FPR or 1-specificity). These parameters are defined as

$$TPR(t) = \frac{TP(t)}{TP(t) + FN(t)} = Sensitivity(t) \tag{22}$$

$$FPR(t) = \frac{FP(t)}{TN(t) + FP(t)} = 1 - Specificity(t) \tag{23}$$

and are both a function of the decision (detection) threshold, t . The algorithms predictive capability is quantified by computing the “area under the ROC” (AUROC) curve [56,66]. Its predictive power increases as the AUROC approaches 1.0 and decreases as the AUROC approaches 0.0. An AUROC of 0.5 is equivalent to randomly selecting an outcome. The objective of any classification algorithm is to maximize the AUROC. The accuracy and precision of the algorithm represent a measure of its ability to consistently estimate the true outcome of an event. These metrics are estimated using

$$Accuracy(t) = \frac{TP(t) + TN(t)}{TP(t) + TN(t) + FP(t) + FN(t)} \tag{24}$$

$$Precision(t) = \frac{TP(t)}{TP(t) + FP(t)} \tag{25}$$

where both expressions are a function of t .

The prediction power of the forecasting algorithm is characterized using a bootstrapped, leave-one-out (LOO), cross validation methodology. This process requires the removal of one sample from the training data, regeneration of the statistical model using the remaining data, and prediction of the outcome of the removed sample via the new model. Cross validation for each forecasting stage was conducted using 50,000 bootstrapped datasets. This is repeated for each sample in the training set for a collection of detection thresholds that range between 0.0 and 1.0. If the resulting probability is greater than or equal to the threshold, the outcome of the event is declared to be true. If the probability is less than the threshold, the outcome of the event is declared to be false. Since the outcome of each of the training events is known, the number of TP, TN, FP, and FN detections can be determined as a function of the detection threshold and plotted in ROC space.

ROC curves for the intrusion, eruption, and intensity event tree nodes are shown in Figures 5–7. In each plot, the blue line represents the nodes forecasting capability and the black line is the ROC resulting from randomly guessing an outcome. Optimum detection thresholds for each stage of the algorithm are determined from the point on the ROC curve that is closest to the point of perfect classification (0,1), which represents the best trade-off between the TPR and FPR. AUROC estimates for the intrusion, eruption, and intensity nodes are 0.78, 0.81, and 0.80, respectively. These results suggest the algorithm has good forecasting capabilities.

Figure 5. Receiver Operating Characteristics for the intrusion event tree node. The AUROC value of approximately 0.78 suggests this node will have fair to good predictive capabilities. TPR, FPR, accuracy, and precision estimates of 71%, 29%, 71% and 85% are obtained at the optimum detection threshold, (0.91).

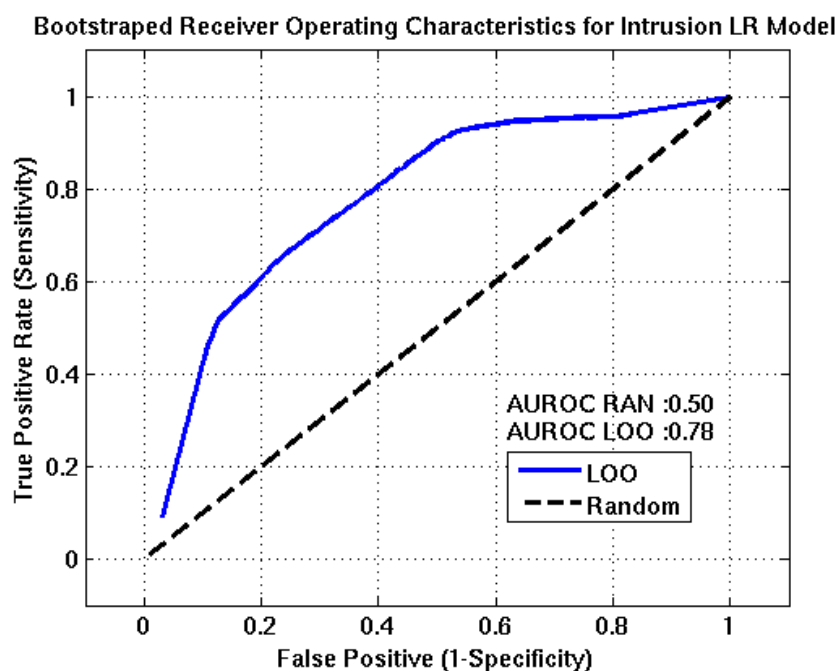


Figure 6. Receiver Operating Characteristics for the eruption event tree node. The AUROC value of approximately 0.81 suggests this node will have fair to good predictive capabilities. TPR, FPR, accuracy, and precision estimates of 75%, 21%, 78%, and 74% are obtained at the optimum detection threshold, (0.47).

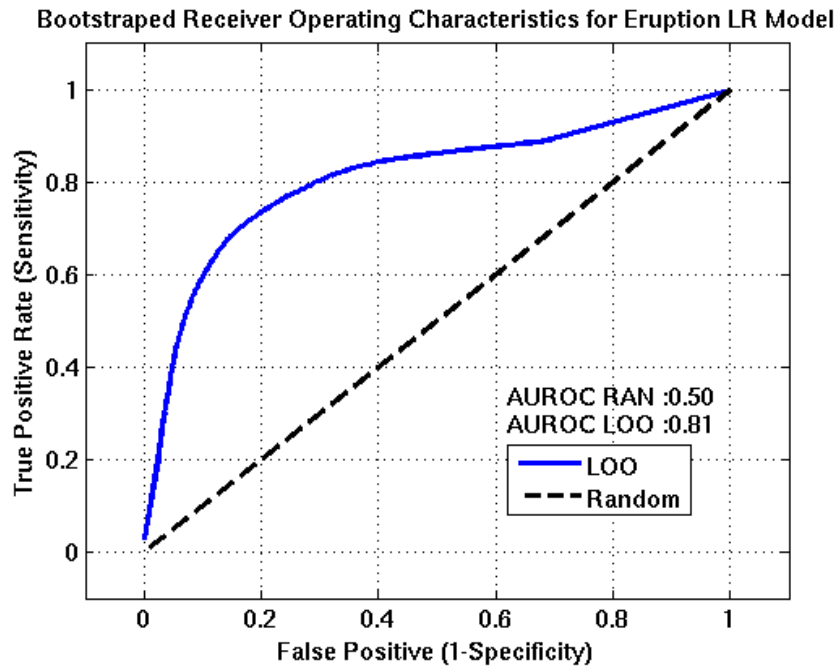
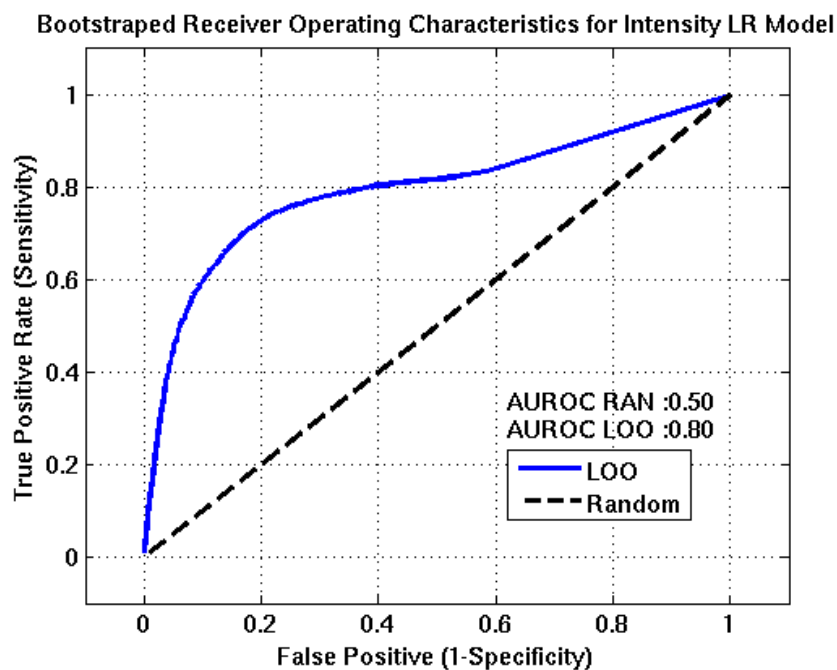


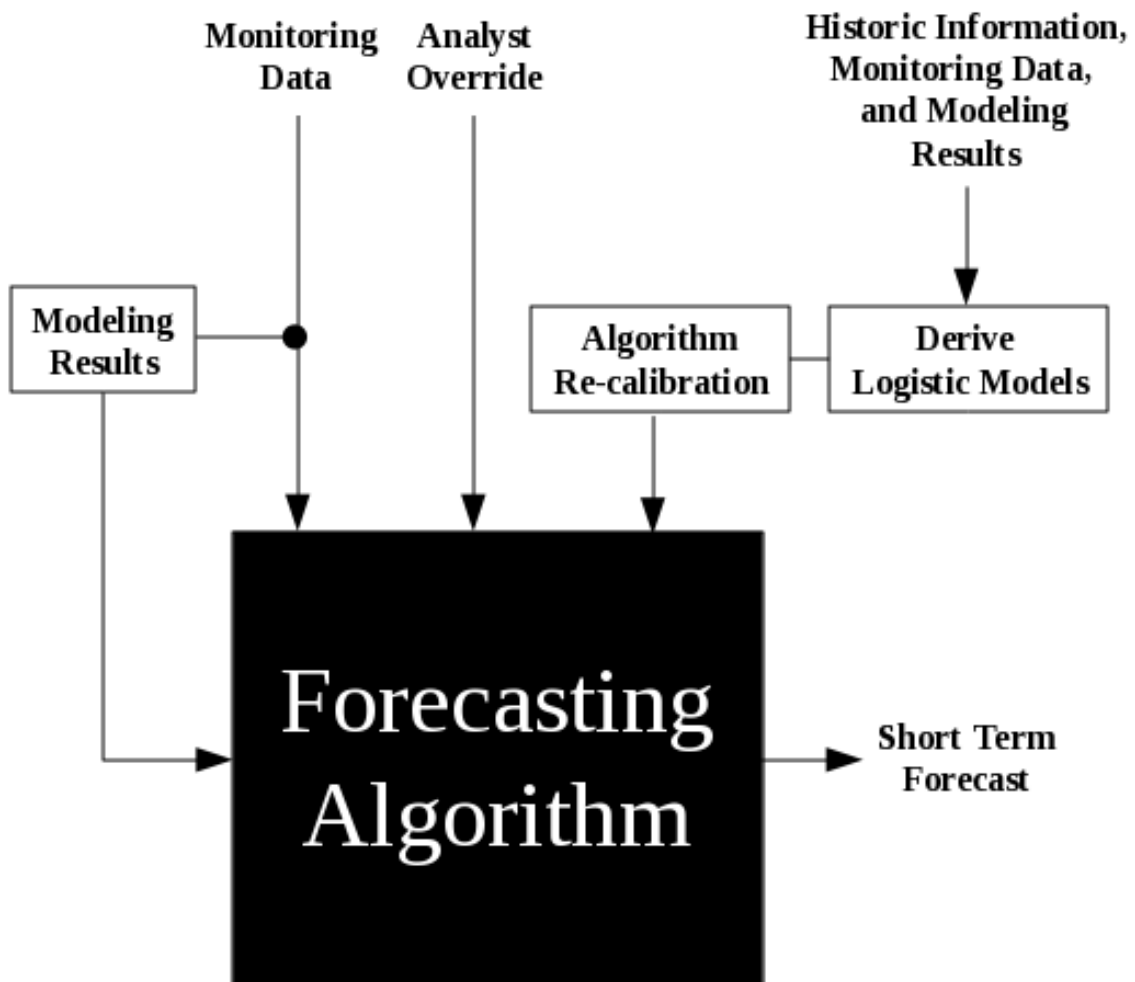
Figure 7. Receiver Operating Characteristics for the intensity event tree node. The AUROC value of approximately 0.80 suggests this node will have fair to good predictive capabilities. TPR, FPR, accuracy, and precision estimates of 73%, 19%, 78%, and 70% are obtained at the optimum detection threshold, (0.21).



2.7. Algorithm Implementation

Block diagrams highlighting the functionality of the forecasting algorithm are shown in Figures 8 and 9. Once the process is initiated at a selected volcano, it searches all available monitoring and modeling data for outliers on a day-by-day basis. As data are fed into the algorithm, the user has the option to use the information to model the source of an event. Once the source has been determined, the modeling input parameter (X_{MM}) is set to 1 if the unrest is the result of a magmatic intrusion or 0 otherwise. In addition, the algorithm provides a mechanism for a human analyst to override any of the automated results. This allows the analyst to introduce information that may not have been accounted for in the algorithm’s decision making process (e.g., personal experience or information not included in the training data).

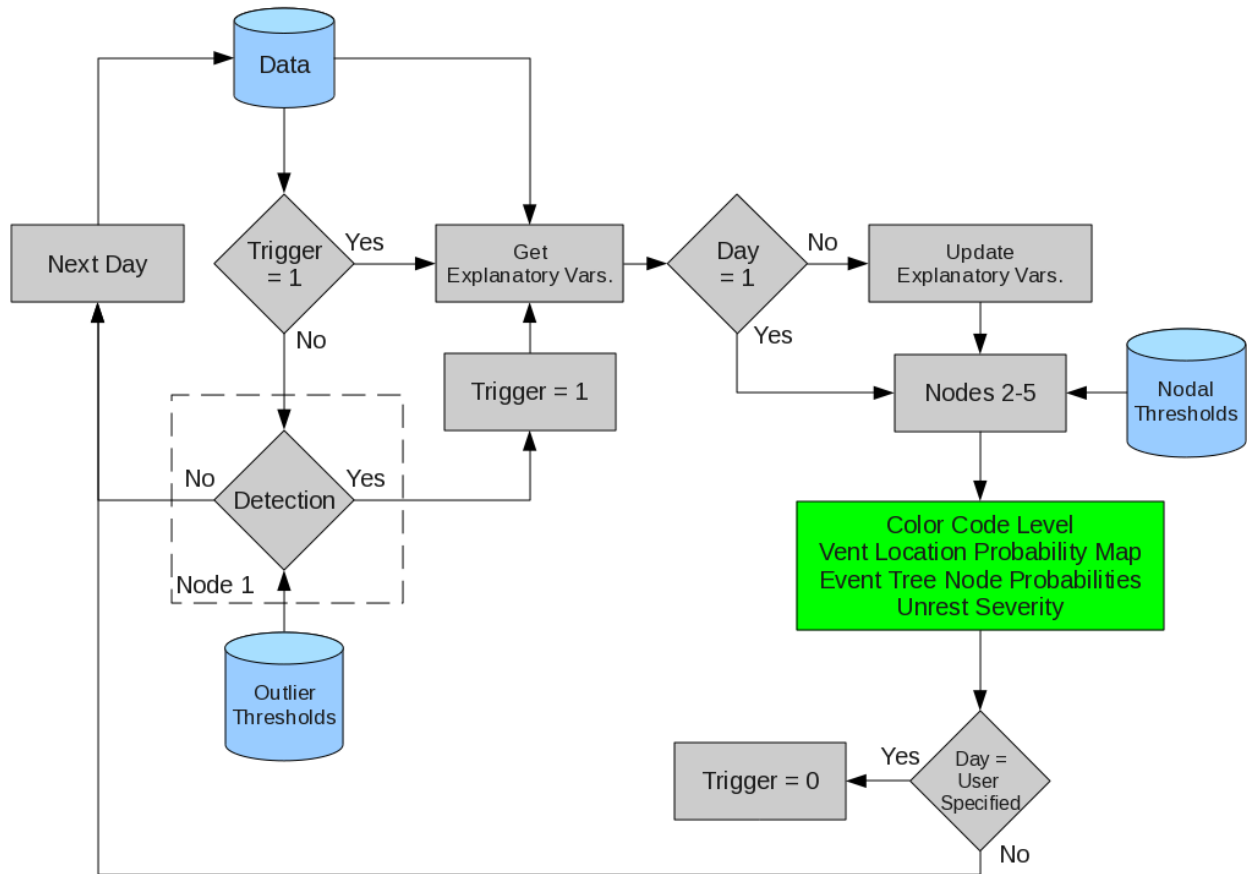
Figure 8. Schematic diagram showing the data flow to and from the forecasting algorithm.



Upon the detection of unrest, the algorithm’s trigger state vector transitions from 0 to 1. While in the trigger state, data corresponding to the appropriate explanatory variables is routed directly to nodes 2–5 for a user specified number of days. During this time the algorithm produces probability estimates for each node, a daily color coded hazard declaration, an unrest severity estimate, and a vent location

probability map. Once the specified number of days has been reached, the trigger states returns to 0, and outlier detection is reinitialized.

Figure 9. Internal functionality of the forecasting algorithm, where gray indicates processes internal to the algorithm, blue represents external data sources, and green identifies products.



The logistic models can be recalibrated upon the introduction of new samples into the training dataset. Once the models have been redefined and validated, the old models are replaced, and the new functionality is instantly available at all sites being monitored. This guarantees that all forecasting results are derived from the most recent set of logistic models.

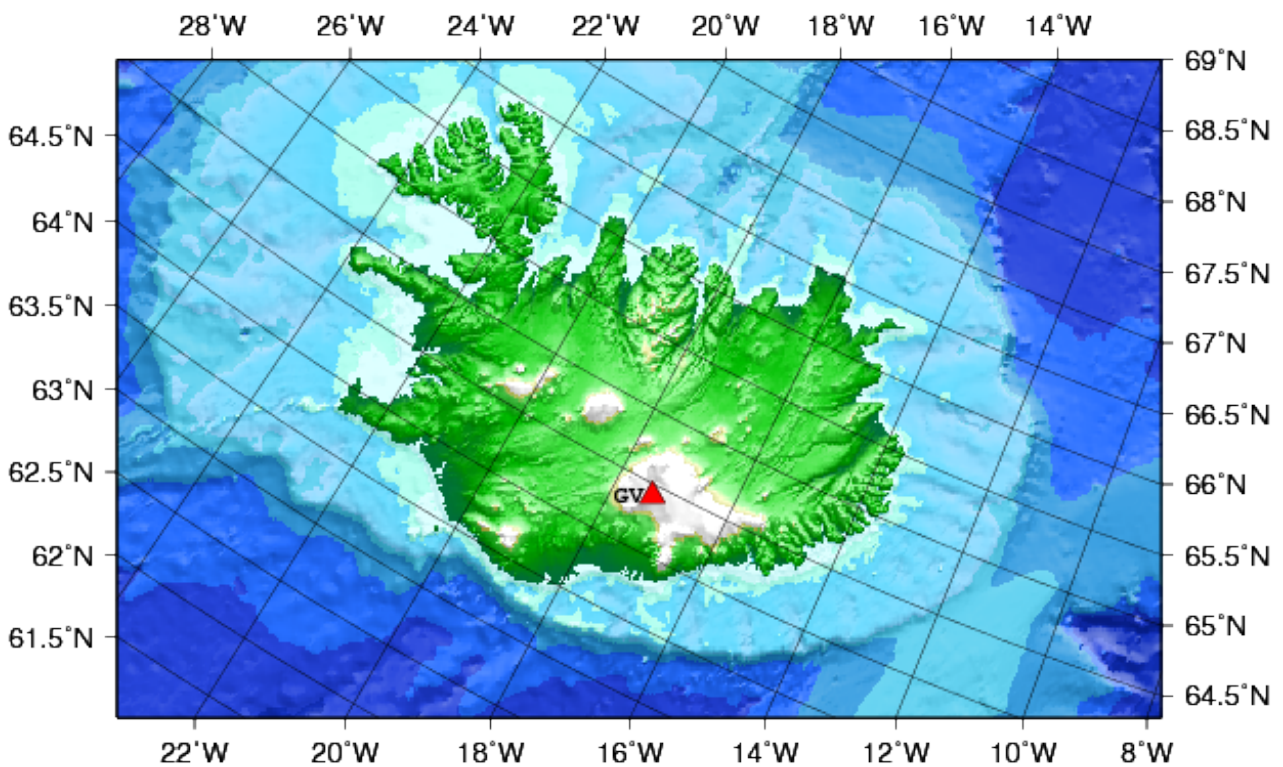
3. Results and Discussion

The volcanic eruption forecasting algorithm (VEFA) was tested against unrest episodes occurring at four volcanoes; Grimsvötn, Okmok, Yellowstone National Park, and Mount Saint Helens. A detailed discussion of forecasts generated for the Icelandic example is presented, since it best illustrates the mechanics of our process. Results from all four examples are compared to forecasts generated by the Bayesian Event Tree Eruption Forecasting (BETEF) 2.0 application [9]. It should be noted that in each of the examples below, algorithm and episode day represent the number of days since initiation of the algorithm and the transition of the trigger state from 0 to 1.

3.1. Grimsvötn Volcano, Iceland

Grimsvötn is located in Iceland approximately 200 m below the northwestern portion of the Vatnajökull icecap (See Figure 10). This volcano is among the most active in Iceland. It has erupted 29 times over the last 211 years, where five have occurred within the last 100 years (e.g., 1938, 1983, 1998, 2004, and 2011) [62]. Its 2011 eruption began on 21 May 2011, nearly 13 months after the now infamous 2010 Eyjafjallajökull eruption. Like its predecessor, it produced large ash clouds that extended 20 km into the atmosphere and disrupted European air traffic for several days [67].

Figure 10. Location of the Grimsvötn Volcano (red triangle).



Since Grimsvötn is a subglacial volcano, GPS data is used to identify deformation consistent with a magmatic intrusion. GPS data acquired by Icelandic Meteorological Office stations posted on the Icelandic Institute of Earth Science (IES) website was used to estimate the source parameters for this episode [68,69]. The GPS stations (GRIM and GFUM) are located about 3 km from the center of the Grimsvötn caldera. Both sensors show continuous uplift at the site following the 2004 eruption, which increases at an almost linear rate between 2005 and 2011. This same pattern of activity was also observed for the five years before the 2004 eruption.

Surface deformation was modeled using a spherical source in a semi-infinite elastic half space. The vertical and radial displacements at the surface are given by

$$\Delta h(r) = C \frac{d}{(r^2 + d^2)^{\frac{3}{2}}} \tag{26}$$

$$\Delta r(r) = C \frac{r}{(r^2 + d^2)^{\frac{3}{2}}} \tag{27}$$

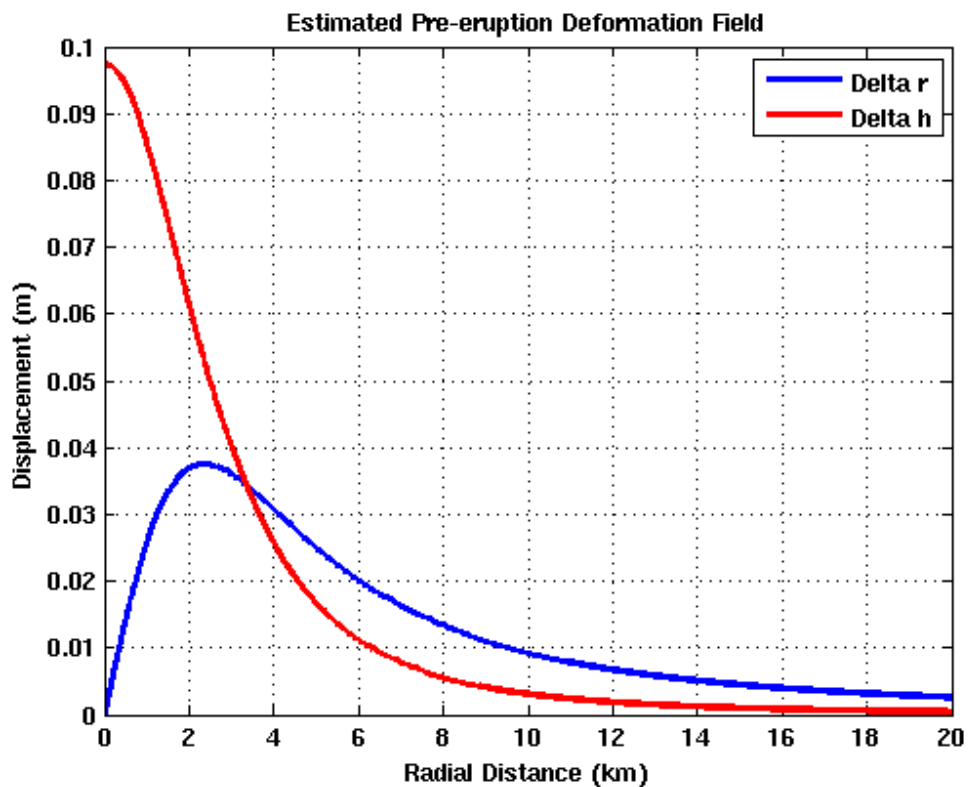
where r is the radial distance from the source, d is the source depth, and C is a scale factor [70]. The intrusion depth was determined by taking the ratio of Equations 26 and 27 and solving for d , which is computed via $(\Delta h(r)/\Delta r(r))r = d$. Vertical and horizontal displacements are measured directly from the GPS records and the location of the intrusion is assumed to reside beneath the caldera center (*i.e.*, $r = 3.0$ km). Resulting source parameters derived eight months before and one month after the 2011 eruption are shown in Table 4. The analysis techniques and assumptions used to determined the source parameters for this episode are similar to those used to study the 1998 eruption [25].

Table 4. Estimated Mogi source parameters derived from GFUM 240 days before and 30 days after the 2011 Grimsvötn Eruption, where positive or negative values of C indicate uplift or subsidence.

| Sample | Δh | Δr | d | C |
|---------------|------------|------------|---------|-------------------------|
| Pre-eruption | 40 mm | 36 mm | 3.33 km | 0.0011 km ³ |
| Post-eruption | 250 mm | 468 mm | 1.60 km | −0.0061 km ³ |

The vent location search area is defined using Equation 26 and the pre-eruptive source parameters shown in Table 4. Resulting deformation profiles are shown in Figure 11. Based on the modeling results, a search radius of 17 km is used to constrain the vent location process, which is the point where the displacement profiles begin to approach zero.

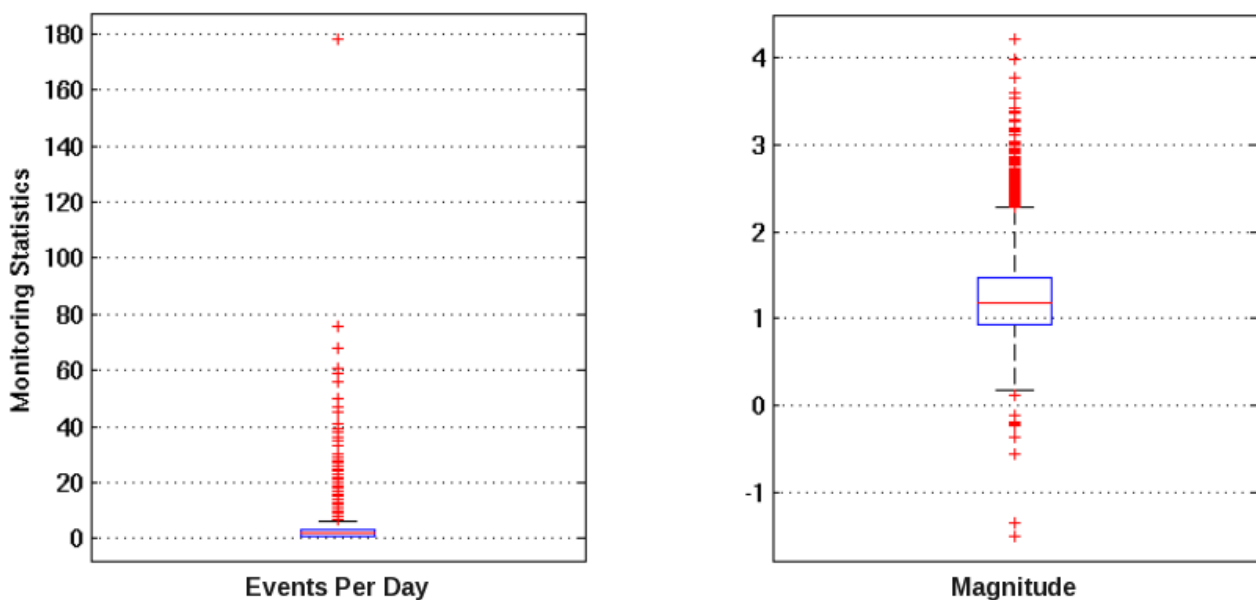
Figure 11. Modeled deformation field preceding the 2011 Grimsvötn eruption.



3.2. Forecasts Preceding Grimsvötn's 2011 Eruption

The VEFA was used to assess the probability of volcanic activity at Grimsvötn preceding its 2011 eruption. Since raw GPS data from GFUM is not available in this situation, only seismic data was used for unrest detection. The boxplots shown in Figure 12 represent the distributions of the number of earthquakes per day and the magnitude of all earthquakes between 2005 and 2011. The thresholds used to defined unrest are 8.0 events per day and a magnitude (M_l) of 2.27.

Figure 12. Boxplots highlighting the distribution of seismicity beneath the Grimsvötn caldera between 2005 and 2011, where the events per day and magnitude whiskers are set to 1.5 time the interquartile range. Monitoring thresholds are 8.0 events per day and a m_l of 2.27.



Monitoring was initiated on 24 November 2010 and triggered on an anomalously large seismic event (M_L 3.54) on 25 November 2010. Unrest severity and trigger state vectors are shown in Figure 13 A and B. The rapidly fluctuating unrest severity is caused by elevated periods of anomalous seismicity throughout the episode (See Figure 14 A and B). On algorithm day 134, positive modeling results were injected into the algorithm. This injection was done to simulate potential delays associated with manual source modeling exercises that may be initiated upon the detection of unrest.

Figure 15A shows a time series of intrusion, eruption, and intensity forecasts for each stage of the algorithm. Initially, activity forecasts fluctuate between 0.60–0.80, 0.18–0.20, and 0.04–0.09 for the intrusion, eruption, and intensity estimates. The large variation in forecasts are due to the rapidly changing seismic conditions at the site. Forecast probabilities increase dramatically upon the injection of positive modeling results into the algorithm. Revised forecasts suggest this event has a 0.91 probability of being caused by a magmatic intrusion, a 0.68 probability of culminating to an eruption, and a 0.24 probability of exceeding an intensity of 1.0.

Figure 13. Algorithm state as a function of processing day. (A) Unrest severity estimates per day; (B) Trigger state per day.

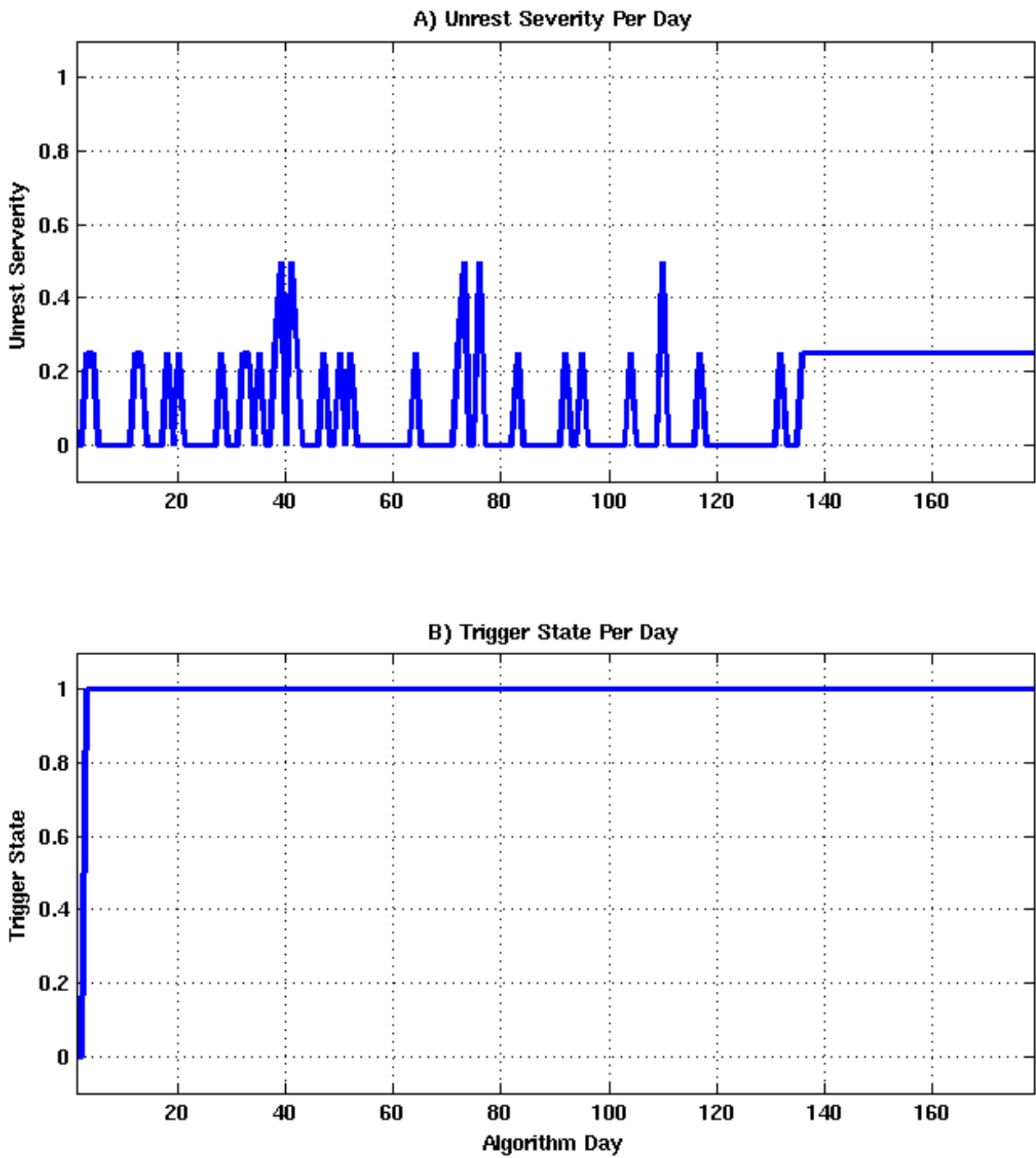
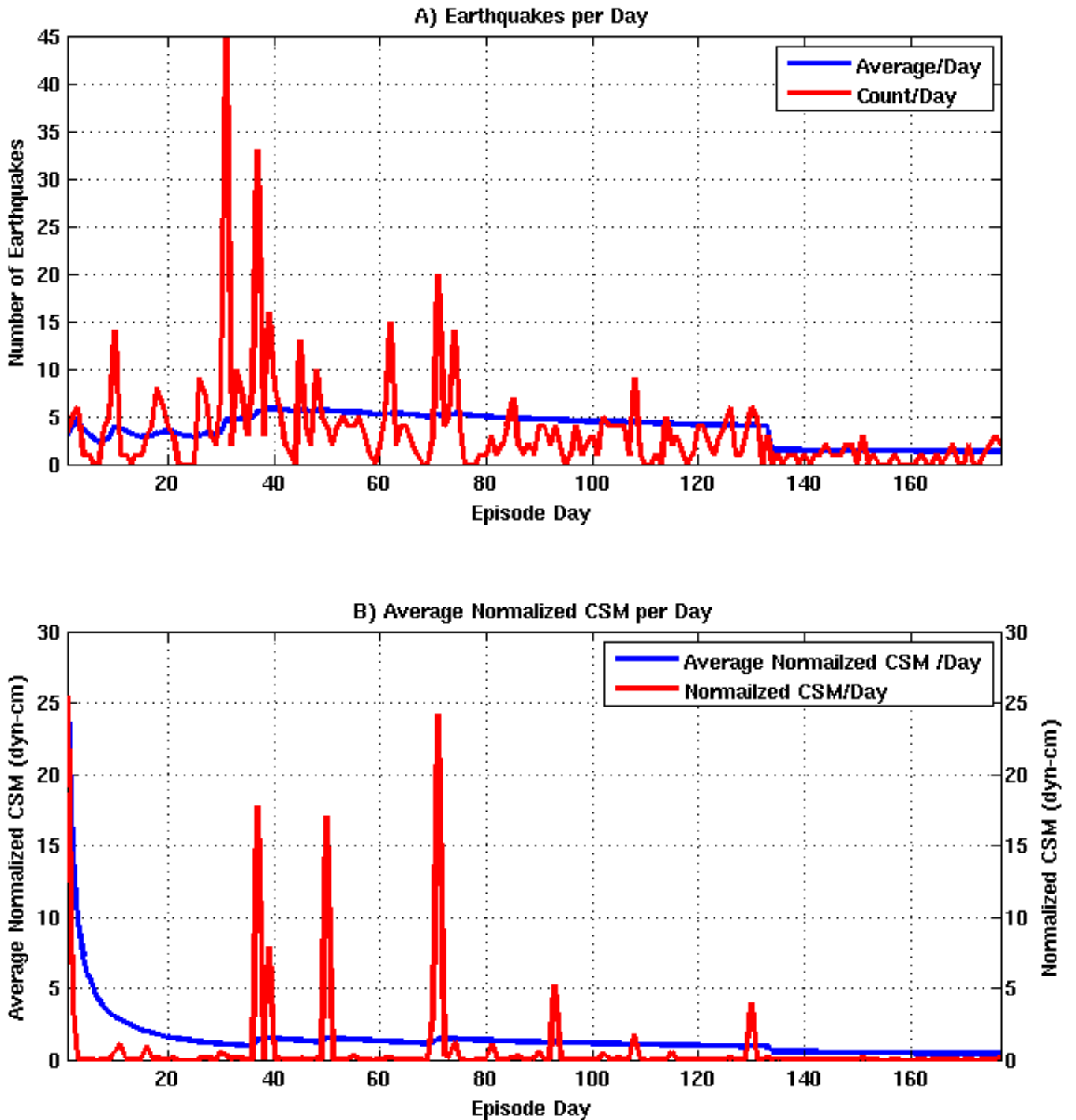
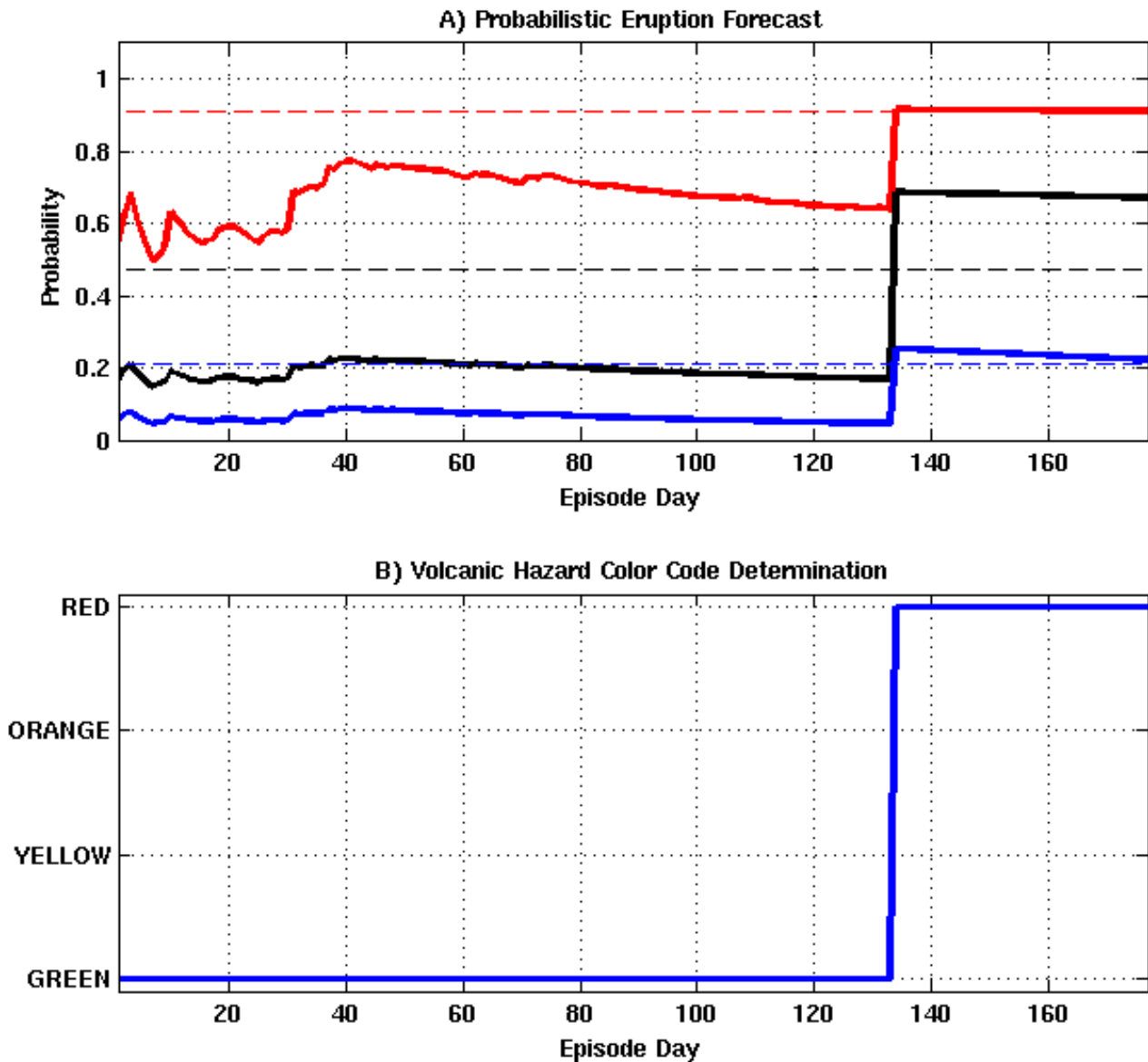


Figure 14. VEFA input parameters. (A) Count and average (X_{NE}) number of earthquakes per episode day (X_{DAYS}), shown in red and blue; (B) Raw and average (X_{CSM}) normalized seismic moment per episode day (X_{DAYS}), shown in red and blue.



The color code declarations shown in Figure 15 B change dramatically over the course of the episode. Initial results place the hazard level as green. Upon the determination that the event is the result of a magmatic intrusion, the hazard level immediately transitions to red. This declaration suggests that an eruption of VEI greater than 1.0 may be imminent.

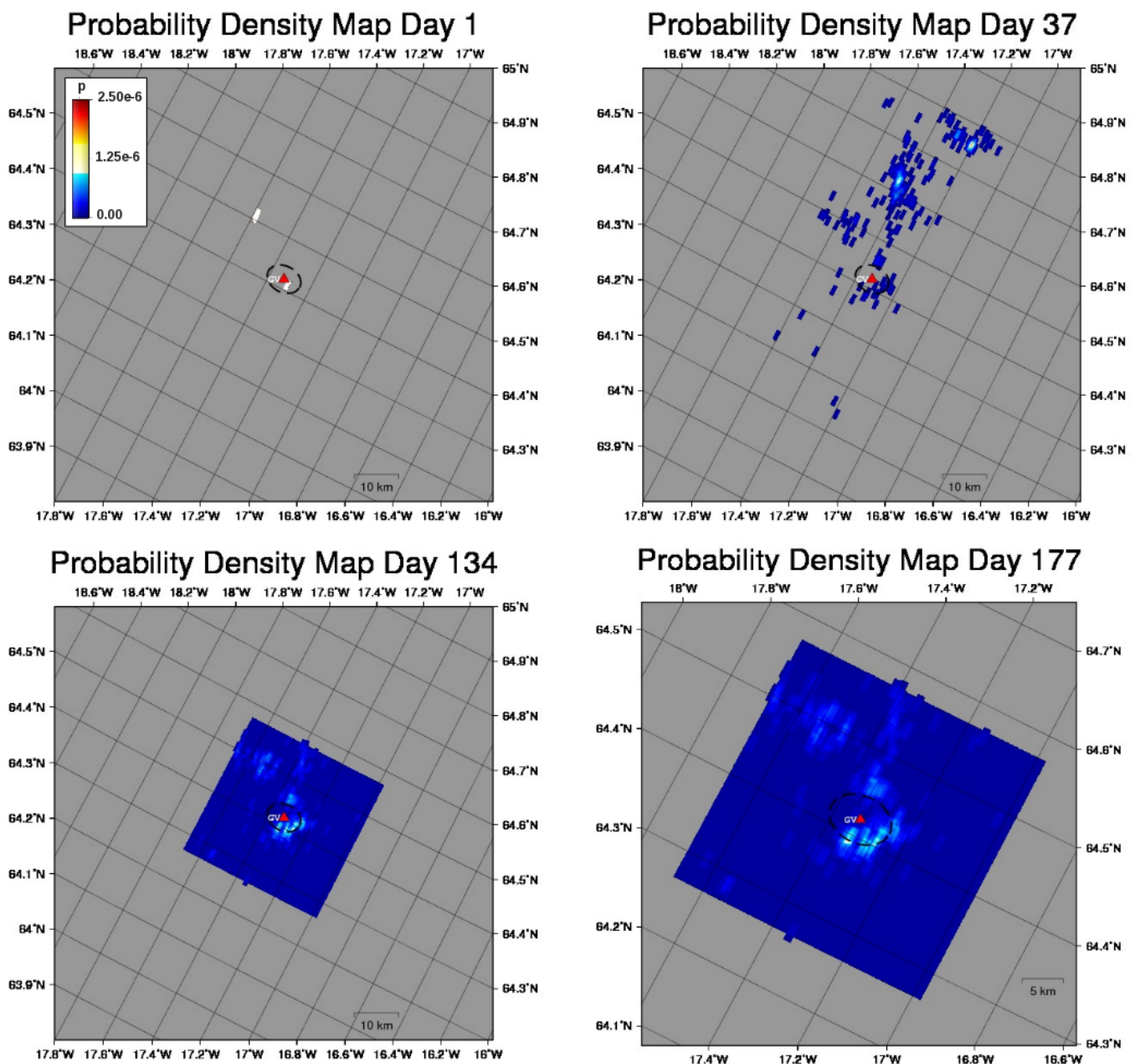
Figure 15. Forecasts of volcanic activity preceding Grimsvötn 2011 eruption, where the intrusion, eruption, and intensity probabilities and thresholds are shown by the red, black, and blue, solid and dotted lines. Introduction of positive modeling results occurs on episode day 134. (A) Probability of occurrence for event tree nodes; (B) Volcanic hazard color code declaration.



A time series of selected spatial PDFs highlighting probable volcanic vent locations at Grimsvötn are shown in Figure 16. Here the spatial resolution of the geographic grid is 1 arc-second. Since the average epicenter uncertainty for the Icelandic seismic network is unknown, a value of 2.3 km is assumed for demonstration purposes. Thus, all X_{seis}^j samples within 1.15 km of each epicenter are set to 1. Due to the absence of modeling information, maps for days 1 and 37 show probable vent locations scattered over the Vatnajökull icecap. Initially, the search area spans 2979 km², $J = 7,094,495$, and all $X_{def}^j = 0$. Modeling results shown in Figure 11 suggest that the deformation source is located approximately 3.33 km below the caldera center and has an isotropic radiation pattern with a 17 km radius. This information provides

the justification to quantitatively constrain the PDF to a square search area spanning 1156 km², reduce J to 2,788,920 probable locations, and set all $X_{def}^j = 1$. As seismic activity accumulates over time, the spatial PDF begins to highlight a preferred vent location. Maps computed for day 134 and day 177 show that the most likely area for vent formation is in the south and southeastern portions of the caldera. Grimsvötn’s 2011 eruption occurred in the southern section of the caldera with a VEI greater than 1.0 [71].

Figure 16. Spatial Probability Density Maps for volcanic activity preceding Grimsvötn’s 2011 eruption, where the black ellipse outlines the approximate perimeter of the caldera. The plot for day 177 has been enlarged to emphasize regions with a higher probability of vent formation within the quantitatively constrained area.



4. Comparisons Between Algorithms

The results generated by the VEFA are compared with those derived from the BETEF v2.0 application. The BETEF tool was developed by Warner Marzocchi, Laura Sandri, and Jacopo Selva of the Istituto Nazionale di Geofisica e Vulcanologia (INGV) and is freely available via the internet. It employs the statistical processing methodology described in [7,9]. To use the tool, unique statistical models must be developed for each volcano being monitored. This means each instance of the application uses a set of assumptions and statistical models that are valid only for a specific volcano. These models are non-transportable and have no defined false positive rate or optimized detection threshold. All model weighting coefficients and detection thresholds used by this application are selected subjectively by the user at the time of their development.

The models used for each example were trained using monitoring and modeling data acquired from the most recent unrest episode preceding the event under test. Modeling results (X_{MM}) were included in the BETEF training set to determine their influence on its forecasting capability. Since eruption history is built directly into the BETEF model during the design process, the X_{ERH} parameter is not required as a real time input. Weighting coefficients for all BETEF input parameters (X_{NE} , X_{CSM} , X_{MM} , and X_{DAYS}) were set to 1. All VEFA and BETEF forecasts are based on the same input data to ensure the comparability of results. The median value of the BETEF forecast is used for comparison purposes in all examples shown below. Error estimates were excluded from the comparisons since they are large and typically span the entire probability range.

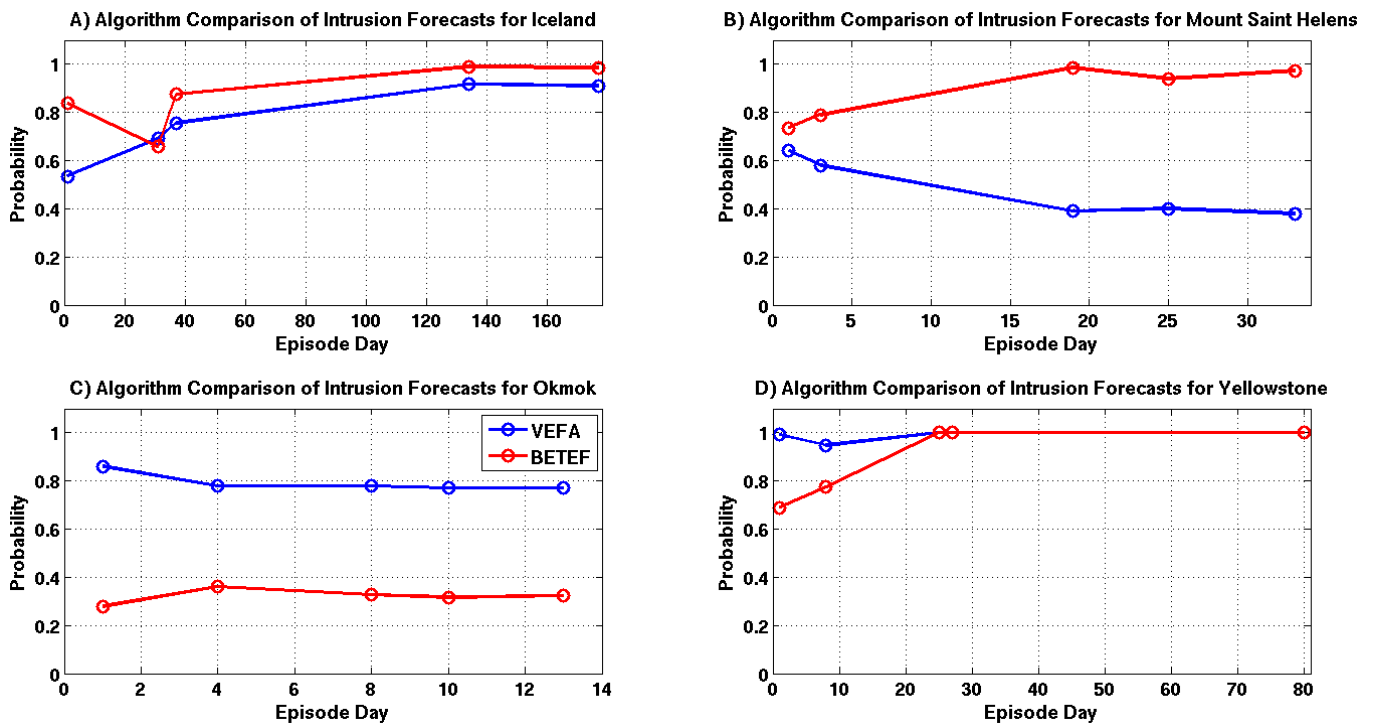
Forecasts for Grimsvötn and three other volcanoes were compared. The additional volcanoes are located in the western portion of North America and frequently exhibit varying forms of unrest. Okmok is an active shield volcano located on the northern portion of Umnak Island in the center of the Aleutian Arc. Comparison forecasts precede Okmok's 2008, VEI 4, eruption. Mount Saint Helens is an active stratovolcano that is situated in the Cascade Mountain Range in the southwestern section of Washington State and last erupted in 2004. Forecasts for Mount Saint Helens are generated over a period of seismic activity in February 2011 that was not due to volcanic unrest. The Yellowstone caldera is located in the Snake River Valley in the northwestern portion of Wyoming and last erupted several thousand years ago. Forecasts for Yellowstone are derived over an unprecedented episode of volcanic unrest that occurred in late 2010. The outcome of each test event and its associated seismicity level, in terms of low or high, is listed in Table 5.

Table 5. Test event outcome for each algorithm stage and associated seismicity level, where 1 or 0 indicates whether the event occurred or not and if seismicity levels were high or low.

| Volcano | Intrusion | Eruption | Intensity (VEI>1) | High Seismicity |
|--------------------|-----------|----------|-------------------|-----------------|
| Grimsvötn | 1 | 1 | 1 | 1 |
| Mount Saint Helens | 0 | 0 | 0 | 0 |
| Okmok | 1 | 1 | 1 | 0 |
| Yellowstone | 1 | 0 | 0 | 1 |

Intrusion forecast comparisons for each example are shown in Figure 17A–D. Intrusion probability estimates for the Grimsvötn and Yellowstone episodes are in very good agreement with one another. However, both of these episodes have a significant amount of associated seismicity which is likely driving the BETEF’s predictions. There are substantial differences between the forecasts for Okmok and Mount Saint Helens. In both cases, the results provided by the VEFA are driven by source modeling results since there is little seismicity associated with these episodes. The supplied modeling information does not appear to influence the BETEF forecasts for Okmok and Mount Saint Helens.

Figure 17. Intrusion probability comparisons for selected episode days, where each time sample is highlighted with a circle and the VEFA and BETEF results are shown in blue and red. (A) Grimsvötn 2011; (B) Mount Saint Helens 2011; (C) Okmok 2008; (D) Yellowstone 2010.



Eruption forecast comparisons are shown in Figure 18A–D. Forecasts generated for the Grimsvötn and Yellowstone episodes are fairly similar. However, this agreement is again most likely due to the high levels of seismicity produced by these episodes. The large difference between the Okmok and Mount Saint Helens forecasts is still observed, where the results differ on average by 0.6 and 0.7, respectively. This discrepancy is likely due to the lack of seismicity associated with these episodes and the VEFA’s ability to properly assimilate source modeling information.

A comparison of eruption intensity estimates are shown in Figure 19A–D. Forecasts for the Yellowstone episode are significantly different, while the results for Grimsvötn, Okmok and Mount Saint Helens show only small differences. The discrepancy in the Yellowstone forecasts are likely due to the VEFA’s knowledge of the source and the high levels of seismicity associated with this episode.

Figure 18. Eruption probability comparisons for selected episode days, where each time sample is highlighted with a circle and the VEFA and BETEF results are shown in blue and red. (A) Grimsvötn 2011; (B) Mount Saint Helens 2011; (C) Okmok 2008; (D) Yellowstone 2010.

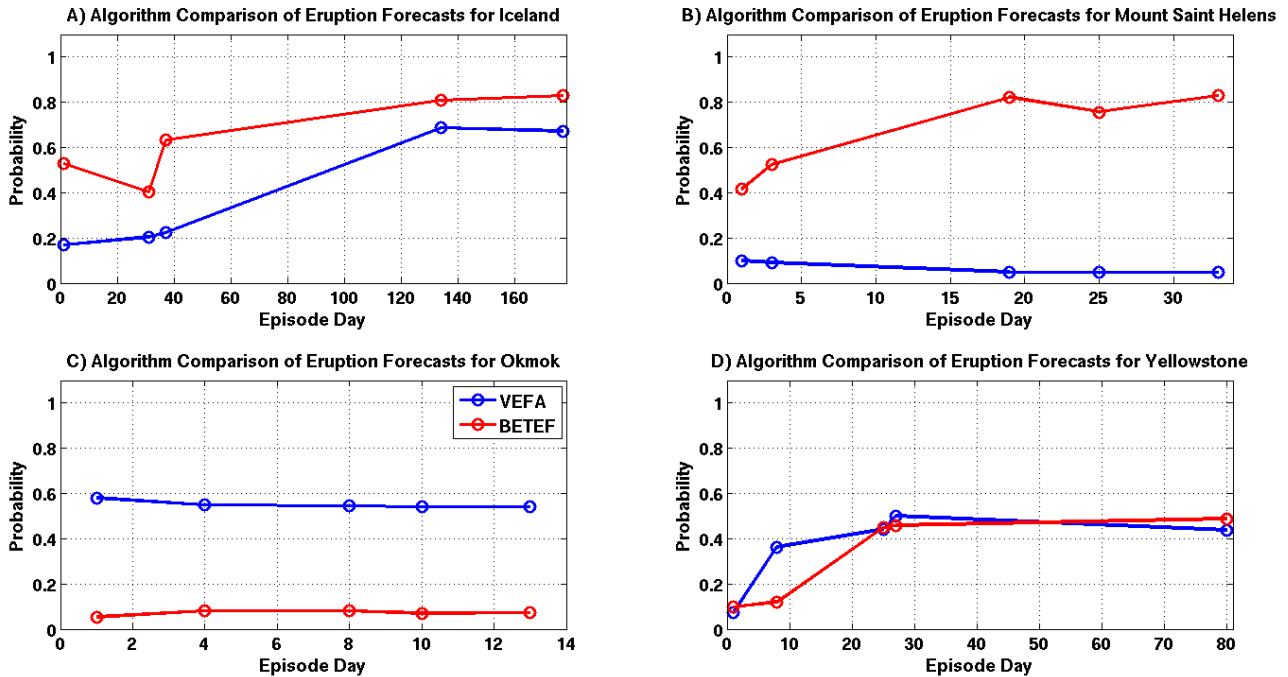
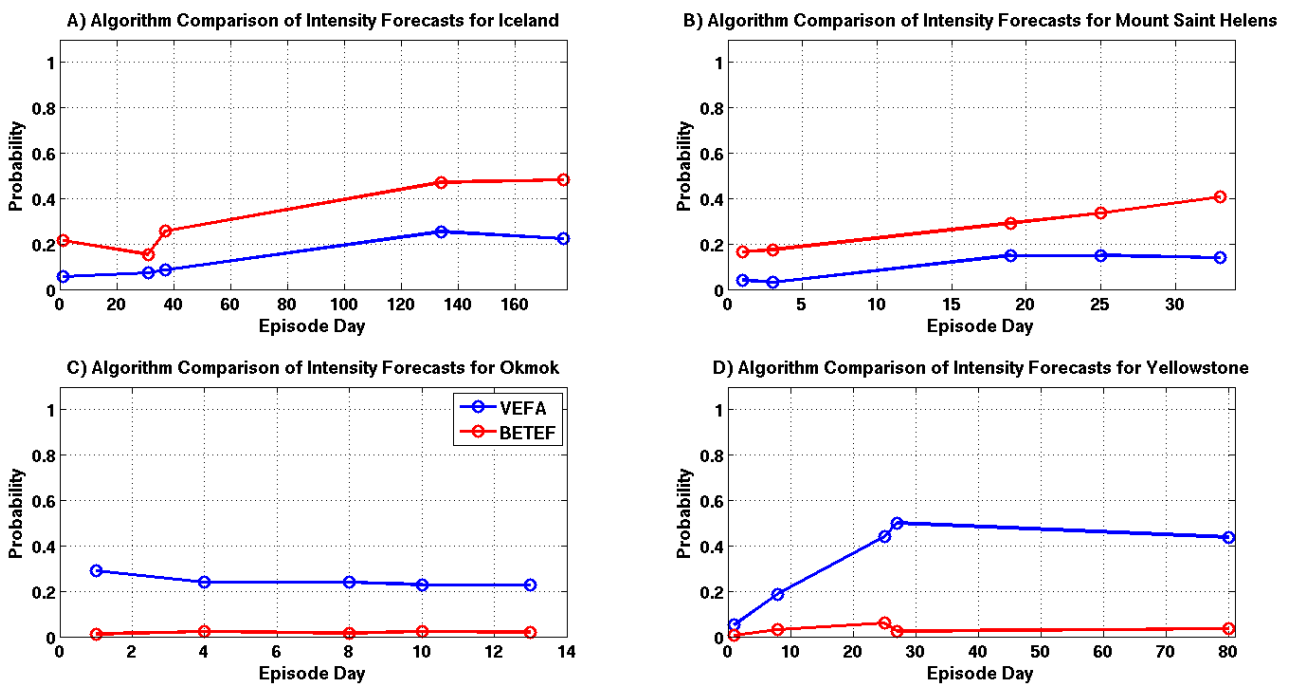


Figure 19. Intensity probability comparisons for selected episode days, where each time sample is highlighted with a circle and the VEFA and BETEF results are shown in blue and red. (A) Grimsvötn 2011; (B) Mount Saint Helens 2011; (C) Okmok 2008; (D) Yellowstone 2010.



5. Summary and Conclusions

An algorithm that forecasts volcanic activity using an event tree analysis system and logistic regression has been developed, characterized, and validated. The suite of logistic models that drive the system were derived from a geographically diverse dataset comprised of source modeling results, monitoring data, and the historic behavior of analog volcanoes. This allows the algorithm to simultaneously utilize a diverse set of information in its decision making process. A bootstrapping analysis of the training dataset allowed for the estimation of robust logistic model coefficients. Probabilities generated from the logistic models increase with positive modeling results, escalating seismicity, and high eruption frequency. The cross validation analysis produced a series of ROC curves with AUROC values in the 0.78–0.81 range, indicating that the algorithm has good forecasting capabilities. In addition, ROC curves also allowed for the determination of the false positive rate and optimum detection threshold for each stage of the algorithm.

Modeling results had a significant influence on the probability estimates for the intrusion and eruption nodes and a moderate effect on the intensity node. Logistic functions illustrated in Figures 2–4 show the influence of modeling information on probabilities decreases between nodes 2, 3, and 4. This result makes sense, because the presence of fluid motion alone does not guarantee escalating volcanic activity. Probability estimates for node 2 should be significantly higher with positive modeling result, since its function is to forecast the presence of fluid motion. However, there is no guarantee an eruption will occur in the presence of fluid motion. Furthermore, the intensity of an eruption is a function of the fluid's chemical composition, accumulation rate, and amount pressure exerted on its storage vessel. Thus the degradation of the modeling results influence on the probability estimates generated by later nodes is consistent with eruption mechanics.

A comparison of the performance between the VEFA and BETEF further illustrates the power of using source modeling information to produce short-term intrusion and eruption forecasts. Source modeling data significantly enhanced the VEFA's forecasting capabilities, especially in situations where little or no associated seismicity exists. This point is confirmed by the differences in the BETEF and VEFA intrusion and eruption forecasts for Okmok and Mount Saint Helens. In both cases, the VEFA leveraged source modeling information to confirm or deny the observed unrest was the result of fluid motion. While the BETEF was also given this information during the development and evaluation of its statistical models, it was unable to make the physical connection between the input data and the source of the unrest. Comparison results suggest that a static suite of empirical statistical models derived from a geographically diverse and sparse dataset are transportable and can compete with, and in some cases outperform, non-transportable empirical models trained exclusively from site specific information. This assessment is supported by comparison results showing that the VEFA forecasts are more consistent with the actual outcome of the test events listed in Table 5.

To the best of our knowledge, this is the first time logistic regression is used to forecast volcanic activity. Furthermore, the derivation of optimized detection thresholds allowed for the quantification of the USGS hazard levels and the determination of an associated false positive rate. This was made possible by the data contained in the volcanic unrest database constructed exclusively for this research. The incorporation of source modeling data into the event tree's decision making process has initiated the

transition of volcano monitoring applications from simple mechanized pattern recognition algorithms to a physical model based system. This paper shows the VEFA has potential for forecasting volcanic activity at various locations throughout the world. Moreover, it can potentially aid civil authorities in determining the proper response to an impending eruption and can be easily implemented by a NVEWS. It should be stressed, however, that this algorithm is meant to assist and not replace the volcanologist in assessing the potential hazard associated with volcanic unrest episodes. Its results should be weighed carefully against a scientist's personal experience and all other available information. It must also be stressed that low probability of occurrence means the event is unlikely, but not impossible. There will be situations where an unlikely event will occur.

Future work will focus on expanding the training dataset. Emphasis will be placed on identifying additional explanatory variables that can further enhance the predictive power of the algorithm. The Earth Observatory of Singapore, Nanyang Technological University, is leading a research initiative to develop a global volcanic unrest database referred to as WOVOdat [72]. This database will contain observations from various monitoring technologies and source modeling results from volcanoes all over the world. However, this database is under construction and is not yet open to the public. Once available, each of the logistic models will be redefined to exploit this diverse and comprehensive database. In addition, comparisons with other decision making techniques such as Classification and Regression Tree (CART) analysis will also be performed.

Acknowledgments

This research was funded, in part, by Florida Space Research Program award 66018006-Y2. Seismic event catalogs used in this study were derived from open catalogs posted on the internet by the USGS, University of Alaska Fairbanks, Alaska Volcano Observatory (AVO), Icelandic Meteorological Office, and the INGV. GPS data was acquired from the Icelandic Meteorological Office and Icelandic Institute of Earth Science websites [68,69]. The advice of Dr. Dale Anderson is greatly appreciated and was instrumental in the successful completion of the bootstrapping study and derivation of logistic coefficients. The maps shown in this report were created with the Generic Mapping Tool (GMT) [73].

References

1. Newhall, C.G. Volcanology 101 for seismologists. *Treatise Geophys.* **2007**, *4*, 351–388.
2. Newhall, C. *A Method for Estimating Intermediate and Long-Term Risks from Volcanic Activity, with an Example from Mount St. Helens, Washington*; Open File Report 82-396; United States Geological Survey: Reston, VA, USA, 1982.
3. Newhall, C. *Semiquantitative Assessment of Changing Volcanic Risk at Mount St. Helens, Washington*; Open File Report 84-272; United States Geological Survey: Reston, VA, USA, 1984.
4. Aspinall, W.P.; Cooke, M.R. Expert Judgement and the Montserrat Volcano Eruption. In *Proceedings of the 4th International Conference on Probabilistic Safety Assessment and Management PSAM4*, New York City, USA, 13–18 September 1998; Volume 3, pp. 2113–2118.
5. Newhall, C.; Hoblitt, R.P. Constructing event trees for Volcanic Crises. *Bull. Volcanol.* **2002**, *64*, 3–20.

6. Aspinall, W.; Woo, G.; Voight, B.; Baxter, P. Evidence-based volcanology: Application to eruption crises. *J. Volcanol. Geotherm. Res.* **2003**, *128*, 273–285.
7. Marzocchi, W.; Sandri, L.; Gasparini, P.; Newhall, C.; Boschi, E. Quantifying probabilities of volcanic events: The example of volcanic hazard at Mount Vesuvius. *J. Geophys. Res.* **2004**, *109*, doi:10.1029/2004JB003155.
8. Marzocchi, W.; Sandri, L.; Selva, J. A Quantitative Model for Volcanic Hazard Assessment. In *Statistics in Volcanology*; Geological Society for IAVCEI: London, UK, 2006; Volume 1, pp. 31–37.
9. Marzocchi, W.; Sandri, L.; Selva, J. BET EF: A probabilistic tool for long and short term eruption forecasting. *Bull. Volcanol.* **2008**, *70*, 623–632.
10. Marzocchi, W.; Sandri, L.; Selva, J. BET VH: A probabilistic tool for long term volcanic hazard assessment. *Bull. Volcanol.* **2010**, *72*, 705–716.
11. Sobradelo, R.; Marti, J. Bayesian event tree for long term volcanic hazard assessment: Application to teide-pico viejo stratovolcanoes, Tenerife, Canary Islands. *J. Geophys. Res.* **2010**, *115*, doi:10.1029/2009JB006566.
12. Lindsay, J.; Marzocchi, W.; Jolly, G.; Constantinescu, R.; Selva, J.; Sandri, L. Towards real-time eruption forecasting in the Auckland Volcanic Field: Application of BETEF during the New Zealand National Disaster Exercise Ruaumoko. *Bull. Volcanol.* **2010**, *72*, 185–204.
13. Poland, M.; Burgmann, R.; Dzurisin, D.; Lisowski, M.; Masterlark, T.; Owen, S.; Fink, J. Constraints on the mechanism of long-term, steady subsidence at Medicine Lake volcano, northern California, from GPS, leveling, and InSAR. *J. Volcanol. Geotherm. Res.* **2006**, *150*, 55–78.
14. Bridges, D.L.; Gao, S.S. Spatial variation of seismic b-values beneath Makushin Volcano, Unalaska Island, Alaska. *Earth Planet. Sci. Lett.* **2002**, *245*, 408–415.
15. Feigl, K.L.; Gasperi, J.; Sigmundsson, F.; Rigo, A. Crustal deformation near Hengill Volcano, Iceland 1993–1998: Coupling between magmatic activity and faulting inferred from elastic modeling of satellite radar interferograms. *J. Geophys. Res.* **2000**, *105*, doi:10.1029/2000JB900209.
16. Lu, Z.; Fatland, R.; Wyss, M.; Li, S.; Eichelberger, J.; Dean, K.; Freymueller, J. Deformation of New Trident volcano measured by ERS-1 SAR interferometry, Katmai National Park, Alaska. *Geophys. Res. Lett.* **1997**, *24*, 695–698.
17. Poland, M.; Bawden, G.; Lisowski, M.; Dzurisin, D. *Newly Discovered Subsidence at Lassen Peak, Southern Cascade Range, California, from InSAR and GPS*; EOS transaction, 2004 Fall Meeting Supplement; American Geophysical Union: Washington, DC, USA, 2004.
18. Hjaltadottir, S.; Vogfjord, K.S.; Slunga, R. *Seismic Signs of Magma Pathways Through the Crust in the Eyjafjallajokull Volcano, South Iceland*; Technical Report VI 2009-013; Icelandic Meteorological Office: Vedurstofa Islands, Reykjavik, 2009.
19. Lu, Z.; Wicks, C.; Power, J.A.; Dzurisin, D. Ground deformation associated with the March 1996 earthquake swarm at Akutan volcano, Alaska, revealed by satellite radar interferometry. *J. Geophys. Res.* **2000**, *105*, 21,483–21,495.
20. Roman, D.C.; Power, J.A. Mechanism of the 1996-97 non-eruptive volcano-tectonic earthquake swarm at Iliamna Volcano, Alaska. *Bull. Volcanol.* **2011**, *73*, 143–153.

21. Lu, Z.; Wicks, C.; Power, J.; Dzurisin, D.; Thatcher, W.; Masterlark, T. Interferometric Synthetic Aperture Radar Studies of Alaska Volcanoes. In *Proceedings of the IEEE International Geoscience and Remote Sensing Symposium*, Toronto, Canada, 24–28 June 2002; pp. 191–194.
22. Wicks, C.W.; Dzurisin, D.; Ingebritsen, S.; Thatcher, W.; Lu, Z.; Iverson, J. Magmatic activity beneath the quiescent Three Sisters volcanic center, central Oregon Cascade Range, USA. *Geophys. Res. Lett.* **2002**, *29*, doi:10.1029/2001GL014205.
23. Owen, S.; Segall, P.; Lisowski, M.; Miklius, A.; Murray, M.; Bevis, M.; Foster, J. January 30, 1997 eruptive event on Kilauea Volcano, Hawaii as monitored by continuous GPS. *Geophys. Res. Lett.* **2000**, *27*, 2757–2760.
24. Lu, Z.; Masterlark, T.; Power, J.; Dzurisin, D.; Wicks, C. Subsidence at Kiska Volcano, Western Aleutians, detected by satellite radar interferometry. *Geophys. Res. Lett.* **2002**, *29*, doi:10.1029/2002GL014948.
25. Sturkell, E.; Einarsson, P.; Sigmundsson, F.; Hreinsdóttir, S.; Geirsson, H. Deformation of Grimsvotn volcano, Iceland: 1998 eruption and subsequent inflation. *Geophys. Res. Lett.* **2003**, *30*, doi:10.1029/2002GL016460.
26. Moran, S.C.; Kwoun, O.; Masterlark, T.; Lu, Z. On the absence of InSAR-detected volcano deformation spanning the 1995–1996 and 1999 eruptions of Shishaldin Volcano, Alaska. *J. Volcanol. Geotherm. Res.* **2006**, *150*, 119–131.
27. Mann, D.; Freymueller, J. Volcanic and tectonic deformation on Unimak Island in the Aleutian Arc, Alaska. *J. Geophys. Res.* **2003**, *108*, doi:10.1029/2002JB001925.
28. Sturkell, E.; Einarsson, P.; Sigmundsson, F.; Hooper, A.; Ofeigsson, B.G.; Geirsson, H.; lafsson, H.O. Katla and Eyjafjallajokull Volcanoes. *Dev. Quat. Sci.* **2010**, *13*, 5–21.
29. Cervelli, P.; Segall, P.; Johnson, K.; Lisowski, M.; Miklius, A. Sudden aseismic fault slip on the south flank of Kilauea volcano. *Lett. Nat.* **2002**, *415*, 1014–1018.
30. Ofeigsson, B.G.; Hooper, A.; Sigmundsson, F.; Sturkell, E.; Grapenthin, R. Deep magma storage at Hekla volcano, Iceland, revealed by InSAR time series analysis. *J. Geophys. Res.* **2011**, *116*, doi:10.1029/2010JB007576.
31. Grapenthin, R.; Ofeigsson, B.G.; Sigmundsson, F.; Sturkell, E.; Hooper, A. Pressure sources versus surface loads: Analyzing volcano deformation signal composition with an application to Hekla volcano, Iceland. *Geophys. Res. Lett.* **2010**, *37*, doi:10.1029/2010GL044590.
32. Pedersen, R.; Sigmundsson, F. Temporal development of the 1999 intrusive episode in the Eyjafjallajokull volcano, Iceland, derived from InSAR images. *Bull. Volcanol.* **2006**, *68*, 377–393.
33. Bonaccorso, A.; Aloisi, M.; Mattia, M. Dike emplacement forerunning the Etna July 2001 eruption modeled through continuous tilt and GPS data. *Geophys. Res. Lett.* **2002**, *29*, doi:10.1029/2001GL014397.
34. Lu, Z.; Dzurisin, D.; Biggs, J.; Wicks, C.; McNutt, S. Ground surface deformation patterns, magma supply, and magma storage at Okmok Volcano, Alaska, from InSAR analysis: 1. Intereruption deformation, 1997–2008. *J. Geophys. Res.* **2010**, *115*, doi:10.1029/2009JB006969.
35. Kwoun, O.I.; Lu, Z.; Neal, C.; Wicks, C. Quiescent deformation of the Aniakchak Caldera, Alaska, mapped by InSAR. *Geology* **2005**, *34*, 5–8.

36. Jones, J.; Malone, S.D. Mount Hood earthquake activity: Volcanic or tectonic origins? *Bull. Seismol. Soc. Am.* **2005**, *95*, 818–832.
37. Patane, D.; Mattia, M.; Aloisi, M. Shallow intrusive process during 2002–2004 and current volcanic activity on Mt.Etna. *Geophys. Res. Lett.* **2005**, *32*, doi:10.1029/2004GL021773.
38. Fournier, T.; Freymueller, J. Inflation detected at Mount Veniaminof, Alaska, with campaign GPS. *Geophys. Res. Lett.* **2008**, *35*, doi:10.1029/2008GL035503.
39. Albino, F.; Pinel, V.; Sigmundsson, F. Influence of surface load variations on eruption likelihood: Application to two Icelandic subglacial volcanoes, Grimsvotn and Katla. *Geophys. J. Int.* **2010**, *181*, 1510–1524.
40. Angelis, S.D.; McNutt, S.R. Degassing and hydrothermal activity at Mt. Spurr, Alaska during the summer of 2004 inferred from the complex frequencies of long-period events. *Geophys. Res. Lett.* **2005**, *32*, doi:10.1029/2005GL022618.
41. Coombs, M.L.; Neal, C.A.; Wessels, R.L.; McGimsey, R.G. *Geothermal Disruption of Summit Glaciers at Mount Spurr Volcano, 20046: An Unusual Manifestation of Volcanic Unrest*; Professional Paper 1732-B; United States Geological Survey: Reston, VA, USA, 2005.
42. Bonaccorso, A.; Bonforte, A.; Guglielmino, F.; Palano, M.; Puglisi, G. Composite ground deformation pattern forerunning the 2004–2005 Mount Etna Eruption. *J. Geophys. Res.* **2006**, *111*, doi:10.1029/2005JB004206.
43. Lisowski, M.; Dzursin, D.; Denlinger, R.P.; Iwatsubo, E.Y. *Analysis of GPS-Measured Deformation Associated with the 2004–2006 Dome-Building Eruption of Mount St. Helens, Washington*; Professional Paper 1750; United States Geological Survey: Reston, VA, USA, 2008.
44. Cervelli, P.F.; Fournier, T.; Freymueller, J.; Power, J.A. Ground deformation associated with the precursory unrest and early phases of the January 2006 eruption of Augustine Volcano, Alaska. *Geophys. Res. Lett.* **2006**, *33*, doi:10.1029/2006GL027219.
45. Neal, C.A.; McGimsey, R.G.; Dixon, J.P.; Manevich, A.; Rybin, A. *2006 Volcanic Activity in Alaska, Kamchatka, and the Kurile Islands: Summary of Events and Response of the Alaska Volcano Observatory*; Scientific Investigations Report 20085214; United States Geological Survey: Reston, VA, USA, 2009.
46. McGimsey, R.G.; Neal, C.A.; Dixon, J.P.; Malik, N.; Chibisova, M. *2007 Volcanic activity in Alaska, Kamchatka, and the Kurile Islands: Summary of Events and Response of the Alaska Volcano Observatory*; Scientific Investigations Report 20105242; United States Geological Survey: Reston, VA, USA, 2011.
47. Lu, Z.; Dzursin, D.; Wicks, C.; Power, J. *Diverse deformation patterns of Aleutian volcanoes from InSAR*; European Space Agency Presentation. Available online: http://earth.esa.int/fringe07/participants/227/pres_227.pdf (accessed on 25 May 2011).
48. Jakobsdottir, S.S.; Roberts, M.J.; Gudmundsson, G.B.; Geirsson, H.; Slunga, R. Earthquake Swarms at Upptyppingar, North-East Iceland: A Sign of Magma Intrusion. *Stud. Geophys. Geod.* **2008**, *52*, 513–528.
49. Chang, W.L.; Smith, R.B.; Farrell, J.; Puskas, C.M. An extraordinary episode of Yellowstone caldera uplift, 2004–2010, from GPS and InSAR observations. *Geophys. Res. Lett.* **2010**, *37*, doi:10.1029/2010GL045451.

50. Fournier, T.J.; Pritchard, M.E.; Riddick, S.N. Duration, magnitude, and frequency of subaerial volcano deformation events: New results from Latin America using InSAR and a global synthesis. *Geochem. Geophys. Geosyst.* **2010**, *11*, doi:10.1029/2009GC002558.
51. Decriem, T.; Arnadóttir, J.D.; Hooper, A.; Geirsson, H.; Sigmundsson, F.; Keiding, M.; Ofeigsson, B.G.; Hreinsdóttir, S.; Einarsson, P.; LaFemina, P.; Bennett, R.A. InSAR and GPS Measurements of the 29 May 2008 South Iceland Earthquake Sequence. In *Proceedings of the Fringe Workshop*, Frascati, Italy, 30 November–4 December 2009.
52. Lu, Z.; Masterlark, T.; Dzurisin, D. Interferometric synthetic aperture radar study of Okmok Volcano, Alaska, 1992–2003: Magma supply dynamics and post-emplacement lava flow deformation. *J. Geophys. Res.* **2005**, *110*, doi:10.1029/2004JB003148.
53. Ruppert, N.A.; Prejean, S.; Hansen, R.A. Seismic swarm associated with the 2008 eruption of Kasatochi Volcano, Alaska: Earthquake locations and source parameters. *J. Geophys. Res.* **2011**, *116*, doi:10.1029/2010JB007435.
54. Sigmundsson, F.; Hreinsdóttir, S.; Hooper, A.; Arnadóttir, T.; Pedersen, R.; Roberts, M.J.; Oskarsson, N.; Auriac, A.; Decriem, J.; Einarsson, P.; *et al.* Intrusion triggering of the 2010 Eyjafjalljökull explosive eruption. *Nature* **2010**, *468*, doi:10.1038/nature09558.
55. Press, S.J.; Wilson, S. Choosing between logistic regression and discriminant analysis. *J. Am. Stat. Assoc.* **1978**, *73*, 699–705.
56. Kleinbaum, D.G.; Klein, M. *Logistic Regression: A Self Learning Text*; Springer: Berlin/Heidelberg, Germany, 2010.
57. Neter, J.; Wasserman, W.; Kutner, M.K. *Applied Linear Regression Models*; Richard, D., Ed.; Irwin, INC.: De Witt, IA, USA, 1989.
58. Samanta, B.; Bird, G.L.; Kuijpers, M.; Zimmerman, R.A.; Jarvik, G.P.; Wernovsky, G.; Clancy, R.R.; Licht, D.J.; Gaynor, J.W.; Nataraj, C. Prediction of preintraventricular leukomalacia Part 1: Selection of hemodynamic features using logistic regression and decision tree algorithms. *Artif. Intell. Med.* **2009**, *46*, 201–215.
59. Chiu, L.S. Estimating the exceedance probability of rain rate by logistic regression. *J. Geophys. Res.* **1990**, *95*, 2217–2227.
60. Lee, S. Application of logistic regression model and its validation for landslide susceptibility mapping using GIS and remote sensing data. *Int. J. Remote Sens.* **2005**, *26*, 1477–1491.
61. Moran, S.C.; Newhall, C.; Roman, D.C. Failed magmatic eruptions: Last-stage cessation of magma. *Bull. Volcanol.* **2011**, *73*, 115–122.
62. Institute, S. Global Volcanism Program Web Page. Available online: <http://www.volcano.si.edu/> (accessed on 20 February 2011).
63. Junek, W.N.; Jones, W.L.; Woods, M.T. Detecting developing volcanic unrest. In *Proceedings of the IEEE Southeast Con.*, Orlando, USA, 15–18 March 2012; pp. 1–4.
64. Weiss, N.A. *Introductory Statistics*; Addison Wesley: Boston, USA, 2007.
65. Junek, W.N.; Jones, W.L.; Woods, M.T. Locating incipient volcanic vents using multidisciplinary remote sensing data and source modeling information. *IEEE Geosci. Remote Sens. Lett.* **2012**, in press.

66. Lasko, T.A.; Bhagwat, J.G.; Zou, K.H.; Ohno-Machado, L. The use of receiver operating characteristic curves in biomedical informatics. *J. Biomed. Inf.* **2005**, *38*, 404–415.
67. Showstack, R. Iceland's Grimsvotn volcano erupts. *EOS Trans. AGU* **2011**, *92*, doi:10.1029/2011EO220003.
68. Icelandic Meteorological Office Website for the 2011 Grimsvotn Eruption. Available online: <http://hraun.vedur.is/ja/vatnajokulsvoktun/english.html> (accessed on 1 November 2011).
69. Institute of Earth Science Website for the 2011 Grimsvotn Eruption. Available online: http://earthice.hi.is/page/ies_GV2011_eruption/ (accessed on 1 November 2011).
70. Mogi, K. Relationships between the eruptions of various volcanoes and the deformations of the ground surfaces around them. *Bull. Earthq. Res. Inst.* **1958**, *36*, 99–134.
71. Sturkell, E.C.; Sigmundsson, F.; Einarsson, P.; Hreinsdottir, S.; Villemin, T.; Geirsson, H.; Ofeigsson, B.G.; Jouanne, F.; Bjornsson, H.; Gudmundsson, G.B.; *et al.* Deformation Cycle of the Grimsvotn Sub-Glacial Volcano, Iceland, Measured by GPS. In *Proceedings of the Abstract V31H-04 presented at the Fall Meeting, AGU, San Francisco, CA, USA, 5–9 December 2011*.
72. World Organization of Volcano Observatories WOVOdat: A database of volcanic unrest. Available online: <http://www.wovodat.org/> (accessed on 10 October 2011).
73. Wessel, S.; Smith, W. New, improved version of the generic mapping tool released. *EOS Trans. AGU* **1998**, *79*, doi:10.1029/98EO00426.

© 2012 by the authors; licensee MDPI, Basel, Switzerland. This article is an open access article distributed under the terms and conditions of the Creative Commons Attribution license (<http://creativecommons.org/licenses/by/3.0/>).